PHYSICAL REVIEW D **87,** 014002 (2013)

Automated squark and gluino production to next-to-leading order

Dorival Gonçalves-Netto,[1] David López-Val,[1] Kentarou Mawatari,[2] Tilman Plehn,[1] and Ioan Wigmore[3]
[1]*Institut für Theoretische Physik, Universität Heidelberg, Philosophenweg 16, D-69120 Heidelberg, Germany*
[2]*Theoretische Natuurkunde and IIHE/ELEM, Vrije Universiteit Brussel, Belgium*
and International Solvay Institutes, Pleinlaan 2, B-1050 Brussels, Belgium
[3]*SUPA, School of Physics and Astronomy, The University of Edinburgh, Mayfield Road, Edinburgh EH9 3JZ, United Kingdom*
(Received 10 November 2012; published 2 January 2013)

We present completely general next-to-leading order predictions for squark and gluino production at the LHC, based on the fully automated MADGOLEM tool. Without any assumptions on the mass spectrum we predict production rates and examine the structure of the massless and massive QCD and SUSY-QCD quantum corrections. This allows us to quantify theory uncertainties induced by the spectrum assumptions commonly made. Going beyond total rates we compare general fixed-order distributions to resummed predictions from jet merging. As part of this comprehensive study we present the MADGOLEM treatment of ultraviolet, infrared, and on-shell divergences.

DOI: 10.1103/PhysRevD.87.014002 PACS numbers: 12.38.Bx, 12.60.Jv, 14.80.Da

I. INTRODUCTION

With the LHC close to completing its 8 TeV run, models predicting heavy new particles [1] are under intense scrutiny. Experimental searches [2,3] are probing vast parameter regions in the minimal supersymmetric standard model (MSSM), most notably those parts of the squark-gluino mass plane which can be described in terms of gravity mediation [4]. Inclusive searches for the production and decay of squarks and gluinos play a leading role and require an accurate as well as flexible framework for theory predictions. Understanding decay jets as well as QCD jet radiation [5] is a crucial aspect, affecting triggering, rate measurements [6], or kinematic reconstruction. Advanced analysis tools like subjet structures [7] increase the need for precise QCD and jets predictions.

Squark and gluino production to leading order was studied 30 years ago [8]. Next-to-leading order (NLO) QCD corrections were first computed almost 20 years ago [9–11] and made public in the PROSPINO package [12].[1] These calculations substantially reduce the theoretical uncertainties to the 20–30% level. More recently, electroweak corrections [13], resummed predictions [14], and (approximate) next-to-next-to-leading order predictions [15] have been made available, further decreasing the theoretical uncertainties. Essentially all of these precision studies make simplifying assumptions about the squark mass spectrum and focus on improving total cross section predictions.

In this paper we present numerical results as well as the underlying structure of the completely automized MADGOLEM approach to NLO predictions [16–18]. It allows us to go beyond current limitations, like assumptions on the supersymmetric (SUSY) mass spectrum or the focus on total rates. We compute the total and differential NLO rates going through all squark and gluino pair production channels for several benchmark parameter points. We study in detail the structure and numerical impact of the real and virtual QCD and SUSY-QCD effects for each of these channels. Particular emphasis we devote to illustrating the reduction of the theoretical uncertainties in total rates and kinematic distributions as a key improvement of NLO predictions. Finally, we conduct a comprehensive comparison of the fixed-order differential cross sections with those obtained by multijet matrix element merging, including a variation of the renormalization and factorization scales. Many details on the computation and its numerical validation are included in the four Appendixes.

This study, alongside with its earlier squark-neutralino [16] and sgluon pair [17] counterparts, are examples of fully automized NLO computations in TeV-scale new physics models. This kind of automation will significantly enhance the availability of precision predictions for LHC observables in and beyond the standard model [19], at a time when standard new physics scenarios for the LHC are becoming less and less likely. MADGOLEM is an independent, highly modular add-on to MADGRAPH [20,21], benefiting from its event simulation and analysis features. It generates all tree-level diagrams and helicity amplitudes in the MADGRAPH V4.5 framework [20] and relies on the HELAS [22] library for the numerical evaluation. The one-loop amplitudes are generated by QGRAF [23] and GOLEM [24,25]. Supersymmetric counterterms and Catani-Seymour dipoles [26] are part of our model implementation and can easily be adapted for other new physics models. The subtraction of infrared and on-shell [11,27] divergences is completely automized. MADGOLEM is currently undergoing final tests and will be released to the LHC community soon.

II. RATES

As a starting point we systematically analyze squark and gluino production rates at next-to-leading order.

---

[1] All results shown in this paper have been checked to agree with PROSPINO2 wherever applicable.

We entertain all possible production channels at the LHC involving pairs of squarks and gluinos in the final state:

$$pp \to \tilde q\,\tilde q,\ \tilde q\tilde q^*,\ \tilde q\,\tilde g,\ \tilde g\,\tilde g\,. \tag{1}$$

Following the typical decay signature we focus on the dominant first- and second-generation squarks $\tilde q = \tilde u_{L,R}$, $\tilde d_{L,R}$, $\tilde s_{L,R}$, $\tilde c_{L,R}$. The associated quarks we can safely assume to be massless. Moreover, we disregard flavor mixing; i.e., the SUSY-QCD couplings are flavor-diagonal. Further removing this latter assumption is foreseen in the MADGOLEM setup. In our numerical analysis we use the CTEQ6L1 and CTEQ6M parton densities [28]. Unless stated otherwise, we fix both the central renormalization and factorization scales to the average final-state mass $\mu_R = \mu_F = \mu^0 = (m_1 + m_2)/2$. From previous studies, this choice is known to lead to perturbatively stable results [11].

As real corrections we include all channels with a three-particle final state, in which a light parton accompanies the heavy superpartners. The associated infrared divergences we subtract using Catani-Seymour dipoles [26], generalized to include the massive colored SUSY particles. Details on this implementation are included in Appendix A. With the help of a FKS (Frixione-Kunszt-Signer)-like cutoff α [29] we can select the phase space regions covered by the dipole subtraction to include more ($\alpha \to 1$) or less ($\alpha \ll 1$) of the nondivergent phase space. Our default choice is $\alpha = 1$, but the total rates must not change with varying α.

Virtual corrections include the one-loop exchange of virtual gluons and gluinos. The standard 't Hooft-Feynman gauge is employed for internal gluons to avoid higher rank loop integrals. Accordingly, Faddeev-Popov ghosts appear in the gluon self-energy and in the three-gluon vertex corrections. Ultraviolet divergences are canceled by renormalizing the strong coupling constant and all masses. Supersymmetry identifies the strong gauge coupling constant g_s and the Yukawa coupling of the quark-squark-gluino interaction, $\hat g_s$. At the one-loop level dimensional regularization induces an explicit breaking of this symmetry via the mismatch between the two fermionic gluino components and the (2-2ϵ) degrees of freedom of the transverse gluon field. We restore the underlying supersymmetry with an appropriate finite counterterm [11,30]. Details on the renormalization procedure can be found in Appendix D.

Finally, we have to remove potential divergences in the three-body phase space due to intermediate resonant states. An example is the appearance of on-shell gluinos as part of the correction to squark-antisquark production, $qg \to \tilde q\,\tilde g \to \tilde q\tilde q^* q$ [11,27]. In addition to the technical complication of a divergent rate these on-shell states introduce a double counting once we sum all squark and gluino production rates to next-to-leading order. In the standard model a similar problem appears in Wt single top production which requires a separation from top pair production, so our MADGOLEM implementation should benefit standard model processes as well.

Following the PROSPINO scheme we remove on-shell divergences locally through a point-by-point subtraction over the entire phase space. Off-shell pieces in the limit of vanishing particle width are genuine parts of the NLO real emission and hence left untouched. This procedure preserves the gauge invariance of the entire matrix element as well as the spin correlations between the intermediate particles and the final state. The subtraction terms have a Breit-Wigner shape and are automatically generated.

Note that for an actual observable we of course need to combine the pair production and associated production channels. Initial-state jet radiation at the LHC may be as hard as decay jets [5] and thus cannot be distinguished on an event-by-event basis. A detailed account of our on-shell subtraction is provided in Appendix B.

A. Parameter space

The effect of NLO corrections on LHC cross sections varies from production channel to production channel and from one mass spectrum to another. In particular the hierarchy between squark and gluino masses affects the behavior of QCD corrections. In Table I we list a set of conventional mass spectra [31] which in the following we will use to study squark and gluino pair production in some detail. For each of the considered benchmarks, we have generated the corresponding physical SUSY masses and coupling constants from the GUT-scale input values defined in Ref. [31], with the help of SOFTSUSY [32]. Scenarios labeled CMSSM-a.b.c (constrained MSSM) are derived from GUT-scale universality conditions with squark and gluino masses above 1 TeV. Each of them exhibits a different squark-gluino mass hierarchy. The

TABLE I. Squark and gluino masses (in GeV) for different benchmark points.

	$m_{\tilde u_L}$	$m_{\tilde u_R}$	$m_{\tilde d_L}$	$m_{\tilde d_R}$	$m_{\tilde g}$	Mass hierarchy
CMSSM 10.2.2	1162	1120	1165	1116	1255	$\tilde q_R < \tilde q_L < \tilde g$
CMSSM 40.2.2	1200	1168	1202	1165	1170	$\tilde q_R < \tilde g < \tilde q_L$
CMSSM 40.3.2	1299	1284	1301	1284	932	$\tilde g < \tilde q_R < \tilde q_L$
mGMSB 1.2	899	868	902	867	946	$\tilde q_R < \tilde q_L < \tilde g$
mGMSB 2.1.2	933	897	936	895	786	$\tilde g < \tilde q_R < \tilde q_L$
mAMSB 1.3	1274	1280	1276	1289	1282	$\tilde u_L < \tilde u_R < \tilde g$, $\tilde d_L < \tilde g < \tilde d_R$

numerical indexing employed herewith (a) denotes the value of tanβ; (b) denotes one given line $m_0 = c_1 m_{1/2} + c_2$ in the $m_0 - m_{1/2}$ parameter space, where m_0 stands for the soft-SUSY breaking scale common to all the sfermions and the Higgs doublets, while $m_{1/2}$ settles a gaugino soft-breaking mass; and (c) refers to one given $m_{1/2}$ reference point, e.g., starting from $m_{1/2} = 500$ GeV for CMSSM 10.2.1 and spaced in steps of 50 GeV. The benchmark points denoted as mGMSB-# and mAMSB-# represent gauge-mediated and anomaly-mediated supersymmetry breaking, and obey a similar notational setup. For specific details we confer the reader to Ref. [31]. While the entire spectrum including the weak gauginos is very different compared to CMSSM-type scenarios, they are considerably less distinctive when we limit ourselves to light-flavor squark and gluino masses. The position of each of the benchmark points in the squark-gluino mass plane defines a maximal mediation scale for SUSY breaking, but this argument cannot simply be turned around [4].

In Tables II and III we document a comprehensive numerical survey over these MSSM parameters for LHC center-of-mass energies of $\sqrt{S} = 14$ TeV and $\sqrt{S} = 8$ TeV. These cross sections can be used to test MADGOLEM once it is publicly available. Using the general MADGOLEM setup it is possible to separate the squark flavor and chirality in squark pair production and in associated squark-gluino production. The size of the NLO QCD effects we express through the consistent ratio $K \equiv \sigma^{\mathrm{NLO}}/\sigma^{\mathrm{LO}}$, in spite of some well-known problems with the convergence of the leading order (LO) parton densities we will notice below.

Already at the level of total cross sections we confirm a number of well-known general trends which are essentially common to all production mechanisms. First, the significance of the QCD quantum effects manifests itself as sizable K factors spanning the range $K \sim 1.1$–2.4 for 14 TeV center-of-mass energy. For 8 TeV we observe uncomfortably large K factors which have nothing to do with real or virtual QCD corrections. Instead, they indicate poor perturbative behavior of the CTEQ parton densities. These suppress LO production rates of heavy particles with $\mathcal{O}$(TeV) masses, while the NLO predictions are perturbatively stable. This can be checked by comparing the CTEQ rate predictions to other parton densities.

Second, the different color charges of squarks and gluinos as well as their spin are clearly reflected in the production rates. Interactions among color octets will give larger rates than color triplets. Similarly, fermion pairs yield larger cross sections than scalar pairs. This effect is

TABLE II. Total cross sections (in fb) and corresponding K factors for squark and gluino production at $\sqrt{S} = 14$ TeV. The renormalization and factorization scales are chosen as the average final-state mass. The notation $\tilde u\,\tilde d$ indicates the summation over all possible final-state chiralities $\tilde u\,\tilde d = \tilde u_L \tilde d_L + \tilde u_L \tilde d_R + \tilde u_R \tilde d_L + \tilde u_R \tilde d_R$. Symmetry factors 1/2 are automatically included, when applicable.

		$\tilde u_L \tilde u_L$			$\tilde u_R \tilde u_R$			$\tilde u_L \tilde u_R$			$\tilde u\,\tilde d$				
	σ^{LO}	σ^{NLO}	K	σ^{LO}	σ^{NLO}	K	σ^{LO}	σ^{NLO}	K	σ^{LO}	σ^{NLO}	K			
CMSSM 10.2.2	26.2	29.2	1.11	31.0	34.3	1.11	26.2	30.7	1.17	87.7	104.8	1.19			
CMSSM 40.2.2	22.8	26.0	1.14	26.0	29.4	1.13	25.2	30.2	1.20	75.2	91.2	1.21			
CMSSM 40.3.2	14.8	18.1	1.22	15.8	19.1	1.21	23.1	29.9	1.29	49.8	63.6	1.28			
mGMSB 1.2	85.3	97.0	1.14	98.1	110.7	1.13	99.7	120.4	1.21	316.6	387.8	1.22			
mGMSB 2.1.2	73.9	88.7	1.20	87.6	104.5	1.19	113.9	144.5	1.27	293.3	372.6	1.27			
mAMSB 1.3	16.8	18.9	1.13	16.4	18.4	1.12	16.1	19.1	1.19	48.3	58.1	1.20			
		$\tilde u_L \tilde u_L^*$			$\tilde u_R \tilde u_R^*$			$\tilde u_L \tilde u_R^*$, $\tilde u_R \tilde u_L^*$			$\tilde u \tilde d^*$				
	σ^{LO}	σ^{NLO}	K	σ^{LO}	σ^{NLO}	K	σ^{LO}	σ^{NLO}	K	σ^{LO}	σ^{NLO}	K			
CMSSM 10.2.2	3.0	4.6	1.54	3.8	5.8	1.53	4.6	6.0	1.30	16.0	19.3	1.21			
CMSSM 40.2.2	2.5	3.8	1.49	3.0	4.6	1.53	3.7	4.9	1.32	13.1	15.8	1.21			
CMSSM 40.3.2	1.7	2.5	1.44	1.9	2.7	1.44	1.9	2.6	1.33	7.7	9.3	1.20			
mGMSB 1.2	17.8	27.5	1.54	21.9	33.7	1.54	21.1	27.8	1.32	74.1	92.8	1.25			
mGMSB 2.1.2	16.0	23.0	1.44	20.2	29.2	1.45	17.1	22.5	1.32	66.0	81.6	1.24			
mAMSB 1.3	1.6	2.4	1.54	1.5	2.3	1.53	2.2	3.0	1.32	7.7	9.2	1.20			
		$\tilde u_L \tilde g$			$\tilde u_R \tilde g$			$\tilde u_L^* \tilde g$			$\tilde d\,\tilde g$			$\tilde g\,\tilde g$	
	σ^{LO}	σ^{NLO}	K	σ^{LO}	σ^{NLO}	K	σ^{LO}	σ^{NLO}	K	σ^{LO}	σ^{NLO}	K	σ^{LO}	σ^{NLO}	K
CMSSM 10.2.2	78.7	108.6	1.38	87.7	120.3	1.37	2.3	3.8	1.63	58.2	83.6	1.44	23.3	53.4	2.29
CMSSM 40.2.2	93.5	131.3	1.40	101.7	142.3	1.40	2.8	4.6	1.65	68.7	100.5	1.46	41.1	94.5	2.30
CMSSM 40.3.2	159.4	239.5	1.50	165.6	248.2	1.50	5.2	9.0	1.73	116.3	182.0	1.57	249.2	552.9	2.22
mGMSB 1.2	467.0	610.6	1.31	511.4	665.4	1.30	18.7	28.3	1.52	371.2	503.3	1.36	222.8	453.4	2.03
mGMSB 2.1.2	777.0	1077.6	1.39	868.0	1193.9	1.38	33.6	52.5	1.56	638.1	914.6	1.43	849.6	1755.0	2.07
mAMSB 1.3	54.4	78.1	1.44	53.5	77.0	1.44	1.5	2.6	1.71	36.3	54.5	1.50	19.0	46.1	2.42

TABLE III. Total cross sections (in fb) and corresponding K factors for squark and gluino production at $\sqrt{S} = 8$ TeV. All scales are chosen at the average final-state mass.

		$\tilde{u}_L\tilde{u}_L$			$\tilde{u}_L\tilde{u}_R$			$\tilde{u}_L\tilde{u}_L^*$			$\tilde{u}_L\tilde{u}_R^*$, $\tilde{u}_R\tilde{u}_L^*$	
	σ^{LO}	σ^{NLO}	K	σ^{LO}	σ^{NLO}	K	σ^{LO}	σ^{NLO}	K	σ^{LO}	σ^{NLO}	K
CMSSM 10.2.2	3.6	3.8	1.06	2.5	2.8	1.12	0.09	0.16	1.68	0.27	0.36	1.36
CMSSM 40.2.2	2.9	3.2	1.09	2.2	2.6	1.15	0.07	0.12	1.63	0.19	0.27	1.38
CMSSM 40.3.2	1.5	1.7	1.16	1.6	2.0	1.24	0.04	0.06	1.59	0.08	0.11	1.42
mGMSB 1.2	19.7	21.6	1.10	17.1	19.9	1.16	1.1	1.8	1.62	2.2	2.9	1.33
mGMSB 2.1.2	15.9	18.5	1.16	18.8	23.2	1.23	0.9	1.4	1.51	1.7	2.2	1.34
mAMSB 1.3	1.8	1.9	1.08	1.1	1.3	1.14	0.04	0.06	1.72	0.09	0.13	1.40
		$\tilde{u}_L\tilde{g}$			$\tilde{u}_L^*\tilde{g}$			$\tilde{g}\tilde{g}$				
	σ^{LO}	σ^{NLO}	K	σ^{LO}	σ^{NLO}	K	σ^{LO}	σ^{NLO}	K			
CMSSM 10.2.2	3.0	5.2	1.74	0.04	0.09	2.25	0.34	1.19	3.51			
CMSSM 40.2.2	3.8	6.7	1.76	0.05	0.12	2.26	0.74	2.57	3.49			
CMSSM 40.3.2	7.8	14.5	1.85	0.12	0.28	2.33	8.68	26.4	3.04			
mGMSB 1.2	34.9	53.8	1.54	0.7	1.3	1.91	7.29	20.6	2.83			
mGMSB 2.1.2	67.3	108.4	1.61	1.5	2.9	1.93	40.85	112.0	2.74			
mAMSB 1.3	1.8	3.2	1.84	0.02	0.05	2.42	0.25	0.95	3.81			

not only observed in the LO and NLO rates but also in the relative K factor.

Third, both the total LO and NLO cross sections decrease with increasing superpartner masses. Nontrivial effects can for example be understood from the threshold behavior of virtual corrections and the real emission, which may in part overcome the phase space suppression of the NLO diagrams [11]. We will expand on all these aspects later in this section.

B. Squark pair production

Squark pair production can lead to a multitude of final states, which we first classify into two basic categories:

(1) Squark-squark pairs $\tilde{q}\,\tilde{q}$, to leading order mediated by t-channel gluino interchange between colliding quarks. This mechanism is flavor locked, so first-generation squarks will dominate. In particular in proton-proton collisions at large parton-x values this channel will contribute large cross sections because it links incoming valence quarks.

(2) Squark-antisquark pairs $\tilde{q}\tilde{q}^*$ with three distinct subchannels: $q\bar{q}$ annihilation through an s-channel gluon, $q\bar{q}$ scattering via a t-channel gluino, and gg fusion with s-channel and t-channel diagrams. Due to the large adjoint color charge and the higher spin representations involved the gg initial-state dominates at the LHC up to moderate parton-x values. In the absence of flavor mixing, the gluino-induced subchannel is flavor locked to the initial state while the other two are flavor locked within the final state. First- and second-generation squarks will therefore contribute with similar rates. All but the gluino-induced channels will also lead to sbottom and stop pair production [9].

The predicted LO and NLO rates alongside their K factors we document in Tables II and III. The production of squark pairs $\tilde{q}\,\tilde{q}$ yields cross sections of 10 to 100 fb for squark and gluino masses around 1 TeV. The squark-antisquark rates for this mass range are roughly 1 order of magnitude smaller. These cross sections are highly sensitive to the strongly interacting superpartner masses. This is largely due to kinematics, i.e., the different squark masses in each benchmark point. For instance, the production of the lighter right-handed squarks comes with larger production rates than that of their left-handed counterparts. According to Table I this is true for all benchmark points except for mAMSB 1.3. This means that in a squark-(anti)squark sample right-handed squarks will be over-represented. This can be a problem if the NLO computation does not keep track of the different masses of left-handed and right-handed quarks.

In contrast, we see that the K factors barely change between benchmark points, because the bulk of the NLO effects are genuine QCD effects. However, all K factors range around $K \sim 1.2$ for squark-squark production—correspondingly, for squark-antisquark production they render $K \sim 1.2$–1.5 depending on the specific channel. This effect is used by PROSPINO2.1, where the different squark masses only enter at leading order, while the NLO corrections are computed with a universal squark mass. Some sample Feynman diagrams we show in Fig. 1. The supersymmetric QCD corrections including one-loop squark and gluino loops are power suppressed by the heavy particle masses.

We make an interesting observation for squark pairs with different chiralities, e.g., $\tilde{u}_L\tilde{u}_R$. As mentioned above, all $\tilde{q}\,\tilde{q}$ channels proceed via a t-channel gluino. For identical final-state chiralities, the gluino propagator corresponds to a mass insertion—enhancing the LO rates for heavy gluinos. This is not true for $\tilde{u}_L\tilde{u}_R$ production, where we probe the $\not{p}$ term in the gluino propagator. This difference can be read off Table II. The $\tilde{u}_L\tilde{u}_L$ and $\tilde{u}_R\tilde{u}_R$ channels

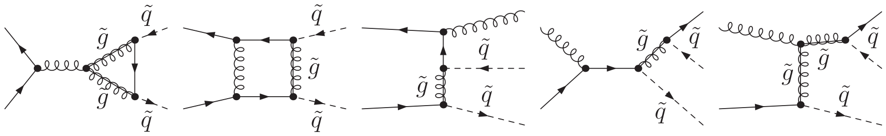

FIG. 1. Sample Feynman diagrams for squark-antisquark production to NLO. Virtual corrections involve the exchange of gluons, gluinos, and squarks. Real corrections denote the emission of one quark or gluon.

are suppressed from CMSSM 10.2.2 to CMSSM 40.3.2, following a decrease in the gluino mass. On the other hand, the $\tilde{u}_L\tilde{u}_R$ rate remains quite constant. This different behavior is also visible from their K factors, which are ordered as $K_{LL} \sim K_{RR} < K_{LR}$.

In Fig. 2 we separate the real and virtual QCD and SUSY-QCD corrections for $\tilde{u}_L\tilde{u}_L^*$ production as a function of the final-state mass $m_{\tilde{u}_L}$. All the other heavy masses we vary simultaneously, keeping the absolute mass splittings of the CMSSM 10.2.2 benchmark point shown in Table I. The two main partonic subprocesses contributing to the process we show separately. The separation into real and virtual corrections we define through Catani-Seymour dipoles with a FKS-like cutoff $\alpha = 1$. The integrated dipoles count towards the virtual corrections while only the hard gluon radiation counts towards the real corrections. This is the reason why the real corrections appear negligible. The cross sections for both the gluon fusion gg and the quark-antiquark $q\bar{q}$ subprocesses are essentially determined by the squark masses and the corresponding phase space suppression. The gluon fusion dominates in the lower squark mass range, contributing with rates of roughly a factor 2 above the $q\bar{q}$ mechanism. Conversely, the gg channel depletes slightly faster than the $q\bar{q}$, especially for large squark masses. This can be traced back to the respective scaling behavior of the cross sections [9] as a function of the partonic energy, and its correlation to the parton luminosities. Indeed, heavier final states probe larger parton-x values—this being the region where the quark parton densities become more competitive, while the gluon luminosity depletes.

The lower panels of Fig. 2 show the relative size of the NLO contributions with respect to the total LO rate. While $\sigma^{\text{virtual}}/\sigma^{\text{LO}}$ grows with increasing squark masses, especially for the gg initial state, $\sigma^{\text{real}}/\sigma^{\text{LO}}$ stays constant. This effect is related to threshold enhancements: first, a long-range gluon exchange between slowly moving squarks in the $gg \to \tilde{u}\tilde{u}^*$ channel gives rise to a Coulomb singularity $\sigma \sim \pi\alpha_s/\beta$, where β denotes the relative squark velocity in the center-of-mass frame, $\beta \equiv \sqrt{1 - 4m_{\tilde{u}}^2/\hat{S}}$. This is nothing but the well-known Sommerfeld enhancement [33]. The associated threshold singularity cancels the leading $\sigma \sim \beta$ dependence from the phase space and leads to finite rates but divergent K factors [11]. In addition, there exists a logarithmic enhancement $\sigma \sim [A\log^2(\beta) + B\log(8\beta^2)]$ from initial-state soft gluon radiation. This second effect is common to the gg and $q\bar{q}$ initial states. Threshold effects can be resummed to improve the precision of the cross section prediction [14].

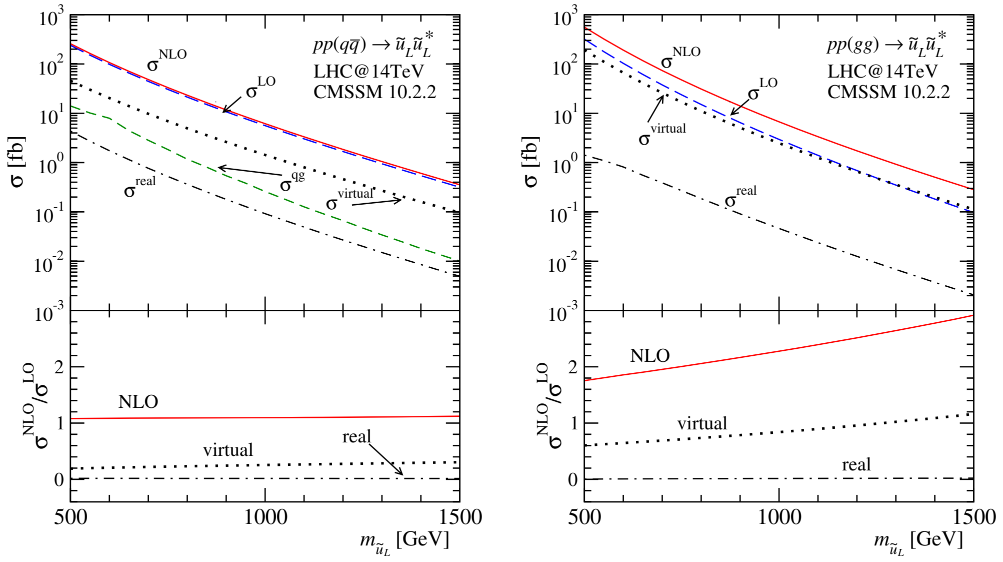

FIG. 2 (color online). Cross sections for $\tilde{u}_L\tilde{u}_L^*$ production for the different initial states as a function of the squark and the gluino masses. The $q\bar{q}$ process (left) includes also the qg crossed channels. Together with $m_{\tilde{u}_L}$ we vary all squark and gluino masses such that the mass splittings of the CMSSM 10.2.2 benchmark point are kept. In the lower panels we evaluate the relative size of the NLO cross section with respect to the total LO rate for each subchannel.

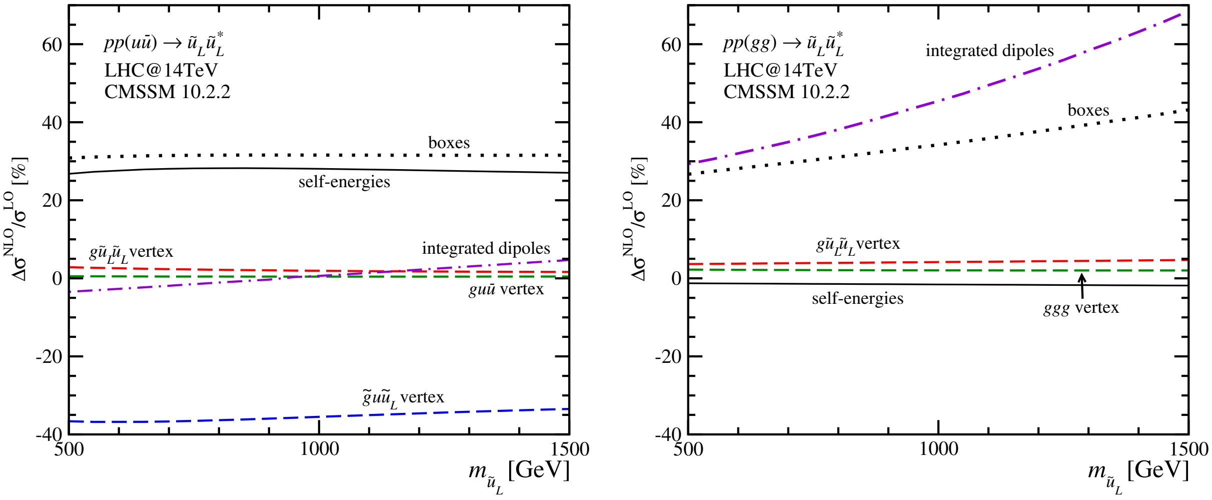

FIG. 3 (color online). Relative shift $\Delta\sigma^{\rm NLO}/\sigma^{\rm LO}$ for the different parts of the virtual corrections to $q\bar{q}/gg \to \tilde{u}_L\tilde{u}_L^*$ production. All squark and gluino masses we vary in parallel, just like in Fig. 2.

The internal architecture of the virtual corrections we analyze in Fig. 3. Virtual diagrams come in different one-loop topologies: self-energy and wave-function corrections, three-point vertex corrections, and box corrections. The box diagrams also include the one-loop corrections to the quartic $gg\tilde{q}\,\tilde{q}$ vertex. Again, we assume the specific flavor/chirality final state $\tilde{u}_L\tilde{u}_L^*$ with the CMSSM 10.2.2 parameter point. Just like in Fig. 2 the masses vary in parallel, keeping the splitting constant. The threshold effects discussed in the previous paragraph are nicely visible in the increasing ratio $\Delta\sigma^{\rm NLO}/\sigma^{\rm LO}$ for the boxes and the integrated dipoles, where the quantity $\Delta\sigma^{\rm NLO}/\sigma^{\rm NLO}$ accounts for the genuine $\mathcal{O}(\alpha_s)$ NLO contributions. This enhancement leads to sizable quantum effects in the 30–70% range for the gg initial state.

For the $q\bar{q}$-initiated subprocess the integrated dipoles are numerically far smaller. The bulk of the virtual corrections are driven by the boxes, the gluino self-energy, and the negative quark-squark-gluino vertex correction. Their remarkable size we can trace back to mass insertions in the gluino-mediated diagrams. Barring these dominant sources, Fig. 3 illustrates that all remaining NLO contributions stay at the ~5% level or below. In the absence of threshold effects, all these pieces are insensitive to the squark mass. As a consequence, both the LO and the NLO cross sections undergo essentially the same phase space suppression as a function of the final-state mass. Because we vary all masses in parallel this is also indicative of the dominance of the gluon-mediated QCD effects as compared to SUSY-QCD corrections. In the large-mass regime the latter have to be power suppressed, matching on to the decoupling regime.

The fact that cross section predictions increase, i.e., exclusion limits become stronger once we include NLO cross sections, is only a superficial effect of the improved QCD predictions. The main reason for higher-order calculations is the increased precision, reflected in the renormalization and factorization scale dependence. As is well known, these scale dependences do not have to be an accurate measure of the theoretical uncertainty. This can be seen for example in Drell-Yan-type processes at the LHC where the LO factorization scale dependence hugely undershoots the known NLO corrections. For the pair production of heavy states mediated by the strong interaction the detailed studies of top pairs give us hope that the scale dependence can be used as a reasonable error estimate.

In Fig. 4 we trace the scale dependences of squark-squark and squark-antisquark production. Note that such a separate scale variation is not possible in PROSPINO, where both scales are identified in the analytic expressions. We profile the behavior of $\sigma^{\rm LO}(\mu)$ and $\sigma^{\rm NLO}(\mu)$ for an independent variation of the renormalization and the factorization scales in the range $\mu^0/10 < \mu_{R,F} < 10\mu^0$. As usual, the central scale choice is $\mu^0 = m_{\tilde{u}_L}$. The path across the μ_R-μ_F plane we illustrate in the little square in the left panel. The numerical results are again given for the CMSSM 10.2.2 parameter point and $\sqrt{S} = 14$ TeV. As expected, the renormalization scale dependence dominates the leading order scale dependence. Unlike in other cases there is no cancellation between the renormalization and the factorization scale dependences. The stabilization of the scale dependence manifests itself as smoother NLO slope. While the LO scale variation covers an $\mathcal{O}(100\%)$ band, the improved NLO uncertainty is limited to $\mathcal{O}(30\%)$. Interestingly, the NLO plateau at small scales is not generated by a combination of the two scale dependences, but is visible for a variation of the renormalization scale alone at fixed small values of the factorization scale.

In Fig. 5 we show the usual LO and NLO cross sections as a function of the final-state mass $m_{\tilde{u}_L}$. The error bar around the central values represents a simultaneous scale variation $[\mu^0/2, 2\mu^0]$. Both error bands nicely overlap and

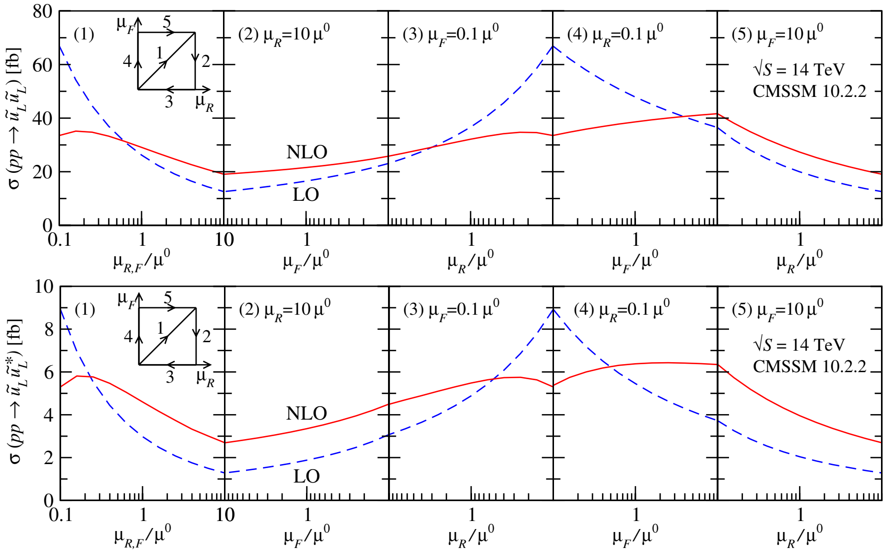

FIG. 4 (color online). Renormalization and factorization scale dependence for squark pair production $pp \rightarrow \tilde{u}_L \tilde{u}_L$ (upper) and $pp \rightarrow \tilde{u}_L \tilde{u}_L^*$ (lower). The plots trace a contour in the μ_R-μ_F plane in the range $\mu = (0.1\text{–}10) \times \mu^0$ with $\mu^0 = m_{\tilde{u}_L}$. All MSSM parameters follow the CMSSM 10.2.2 benchmark point in Table I.

reflect, for $\tilde{u}_L \tilde{u}_L$, a reduction of the theoretical uncertainties from $\mathcal{O}(50\%)$ at LO down to $\mathcal{O}(20\%)$ at NLO—similarly, from $\mathcal{O}(60\%)$ down to $\mathcal{O}(30\%)$ for $\tilde{u}_L \tilde{u}_L^*$.

The most significant upgrade of the MADGOLEM automated framework compared to previous calculations is that we do not have to assume any simplifying relations between the supersymmetric masses. We can freely sweep over the entire parameter space of a given model, varying each of the input parameters independently. This differs from PROSPINO or other precision tools which rely on a single mass scale for all light-flavor squarks for all next-to-leading order effects. A fully general scan as shown in Tables II and III is thus beyond the reach of these tools.

Figure 6 shows quantitative results for this generalized NLO computation. As an example we focus on the (partially inclusive) production of all first-generation squark pairs $pp \rightarrow \tilde{q}\,\tilde{q}$, with $\tilde{q} = \tilde{u}_L, \tilde{u}_R, \tilde{d}_L, \tilde{d}_R$, and examine an independent variation of the different squark masses. In the left two panels we study the effect of a right-left mass separation while identifying s-up and s-charm masses as well as s-down and s-strange masses to the CMSSM 10.2.2 and mGMSB 2.1.2 values shown in Table I. We show the change in the total squark pair cross sections with a growing mass splitting $\Delta m_{R-L} \equiv m_{\tilde{q}_R} - m_{\tilde{q}_L}$, where $\tilde{q} = \tilde{u}, \tilde{d}, \tilde{c}, \tilde{s}$. The results we evaluate in terms of $|\sigma - \sigma_0|/\sigma_0$, where σ_0 denotes the cross section for $\Delta m_{R-L} = 0$. The associated K factor is displayed at the bottom of each panel. In the right panels we show the same analysis for an up-versus-down squark mass splitting $\Delta m_{u-d} \equiv m_{\tilde{u}} - m_{\tilde{d}}$, with $\tilde{u} = \tilde{u}$, $\tilde{c}$ and $\tilde{d} = \tilde{d}$, $\tilde{s}$. The masses of their respective chiral components are separated as in the corresponding benchmark scenarios.

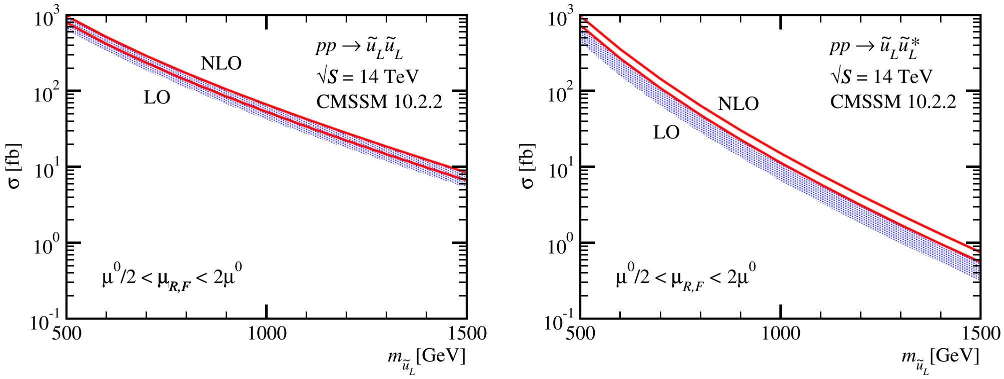

FIG. 5 (color online). Cross sections $\sigma(pp \rightarrow \tilde{u}_L \tilde{u}_L)$ (left) and $\sigma(pp \rightarrow \tilde{u}_L \tilde{u}_L^*)$ (right) as a function of the squark mass. The band corresponds to the scale variation envelope $\mu^0/2 < \mu_{R,F} < 2\mu^0$, where $\mu^0 = m_{\tilde{u}_L}$. The central MSSM parameters are given by the CMSSM 10.2.2 benchmark point. The squark and gluino masses we vary in parallel, just like in Fig. 2.

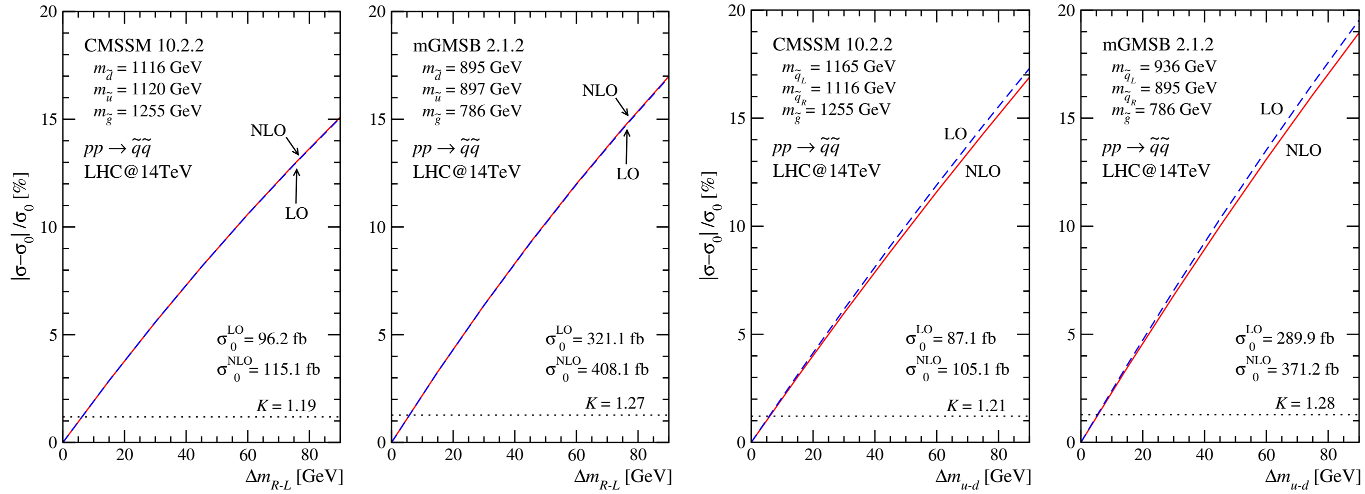

FIG. 6 (color online). Cross sections for squark pair production $pp \to \tilde{q}\,\tilde{q}$ ($\tilde{q} = \tilde{u}_{L,R}, \tilde{d}_{L,R}$) as a function of mass splittings. In the left panels we vary the right-left splitting keeping the flavor splitting constant. In the right panels we vary the $\tilde{u}$-$\tilde{d}$ flavor splitting fixing the right-left splitting. We show the shift with respect to the degenerate spectrum with the masses and the total rates $\sigma_0 \equiv \sigma(\Delta m = 0)$ given in each panel.

The results highlight, first of all, that a fully flexible mass spectrum leaves a measurable footprint in the total cross sections. The rates change by $\mathcal{O}(5\%–20\%)$ for a squark mass splitting of 10–100 GeV, as commonly featured by MSSM benchmark points. These effects lie roughly in the same ballpark as higher-order corrections beyond the fixed next-to-leading order predictions. At the same time, the K factors stay essentially constant with a varying mass splitting. This follows from the fact that while kinematic effects change the cross sections significantly, the NLO corrections are mostly sensitive to mass splittings through SUSY-QCD effects which are typically mass suppressed. For squark pair production, in particular, the NLO rate dependence on Δm_{R-L} and on Δm_{u-d} is affected by the gluino self-energy corrections. Our MADGOLEM results confirm that taking into account the full mass spectrum in the LO rate predictions and reweighting them with a K factor computed most efficiently for a mass-degenerate spectrum gives an accurate estimate of the full NLO rates.

C. Squark-gluino production

Unlike squark or gluino pair production the associated production process does not have a QCD-only component and is always flavor locked, $qg \to \tilde{q}\,\tilde{g}$. This makes it the most model dependent signature. First-generation squarks, mostly $\tilde{u}_{L,R}$, will be copiously produced, and some of the structures will be reminiscent of the electroweak production of squarks with electroweak gauginos, $pp \to \tilde{q}\,\tilde{\chi}$ [16].

Moreover, in this particular channel on-shell divergences can have a twofold origin: they can stem from either an on-shell gluino or an on-shell squark, depending on which of these particles is heavier. This makes associated squark-gluino production the key channel to test our numerical MADGOLEM implementation of automized on-shell subtraction.

We can nicely confirm several qualitative expectations from Tables II and III. For instance, we see how $\tilde{u}_L\tilde{g}$ production dominates over the charge conjugated channel $\tilde{u}_L^*\tilde{g}$, simply due to the valence u quark. This is also the reason why the QCD corrections are larger for the $\tilde{u}_L^*\tilde{g}$ process, because gg-initiated NLO contributions are not suppressed by the relative size of the underlying parton luminosities.

The dependence on the final-state masses we show in Fig. 7, where we display the total cross sections $\sigma(pp \to \tilde{u}_L\tilde{g})$ as a function of the final-state squark mass $m_{\tilde{u}_L}$, noting that the gluino mass is changed together with

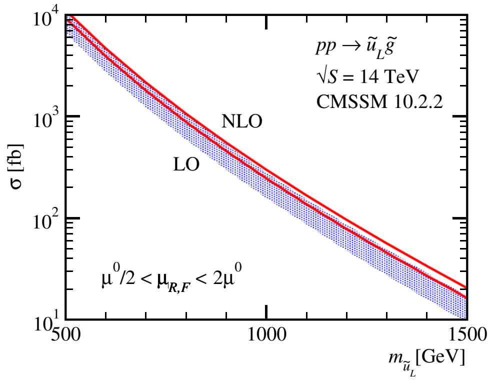

FIG. 7 (color online). Cross sections for $\sigma(pp \to \tilde{u}_L\tilde{g})$ as a function of the squark mass $m_{\tilde{u}_L}$. The band corresponds to a scale variation $\mu^0/2 < \mu_{R,F} < 2\mu^0$, where $\mu^0 = (m_{\tilde{u}_L} + m_{\tilde{g}})/2$. The MSSM parameters are given by the CMSSM 10.2.2 benchmark point. The squark and gluino masses we vary in parallel, just like in Fig. 2.

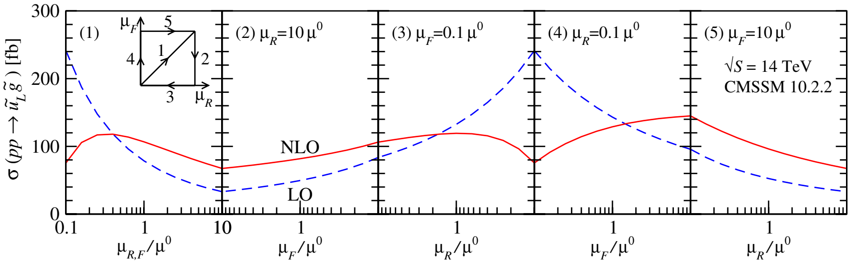

FIG. 8 (color online). Renormalization and factorization scale dependence for $\tilde{u}_L\tilde{g}$ associated production. The plot traces a contour in the μ_R-μ_F plane in the range $\mu = (0.1\text{–}10) \times \mu^0$ with $\mu^0 = (m_{\tilde{u}_L} + m_{\tilde{g}})/2$. All parameters are the same as for Fig. 4, with mass values $m_{\tilde{u}_L} = 1162$ GeV and $m_{\tilde{g}} = 1255$ GeV.

the squark mass. The total cross section is pulled down by roughly 3 orders of magnitude when the final-state mass increases by a factor of 3. We find cross sections as large as $\sigma(\tilde{u}_L\tilde{g}) \sim \mathcal{O}(10)$ pb for $m_{\tilde{u}_L} \lesssim 500$ GeV, which fall down to $\mathcal{O}(10)$ fb for $m_{\tilde{u}_L} \lesssim 1.5$ TeV. A remarkable reduction in scale dependence of $\mathcal{O}(60)\%$ down to $\mathcal{O}(20)\%$ can be assessed by contrasting the LO and NLO uncertainty bands. We provide a complementary viewpoint in Fig. 8, where we probe scale variations of the total cross section as usually in the two-dimensional renormalization vs factorization scale plane.

Finally, we address the effect of a general squark mass pattern on the total rates. Our analysis follows Fig. 6, now for the process $pp \to \tilde{q}\,\tilde{g}$ with $\tilde{q} = \tilde{u}_{L,R}$, $\tilde{d}_{L,R}$. Again, we study the different CMSSM 10.2.2 and mGMSB 2.1.2 scenarios. For each of them, we explore the relative change in the total rate $|\sigma - \sigma^0|/\sigma^0$ when we increase mass splittings from zero (σ_0). We separately examine (i) fixing all left-handed and right-handed squarks at one common mass value and increasing the right-left mass splitting Δm_{R-L}, and (ii) setting a common mass for up-type and down-type squarks and increasing Δm_{u-d}. Similarly to the squark pair case, in Fig. 9 we find variations up to 20% for mass splittings up to $\mathcal{O}(100)$ GeV. The LO and NLO cross sections scale in parallel, with minor differences at the percent level. As expected from the squark pair case the footprint of a nondegenerate squark spectrum factorizes from the QCD corrections, with remaining nonfactorizing effects the level of a few percent.

D. Gluino pair production

Finally, we identify similar phenomenological trends for gluino pair final states. The NLO effects are particularly sizable (cf. Tables II and III) with K factors in the ballpark of ~ 2 for $\sqrt{S} = 14$ TeV, and even surpassing $K \sim 2.5$ for the lower nominal LHC energy $\sqrt{S} = 8$ TeV. These results essentially reproduce what is included in PROSPINO.

The separate dependence on the factorization and renormalization scales we display in Fig. 10. As before, the simultaneous scale variation captures the complete theoretical uncertainty well. Including the NLO corrections significantly reduces the dependence on the renormalization as well as on the factorization scale. In Fig. 11 we show the envelope of the scale variation together with the central LO and NLO rate predictions as a function of the

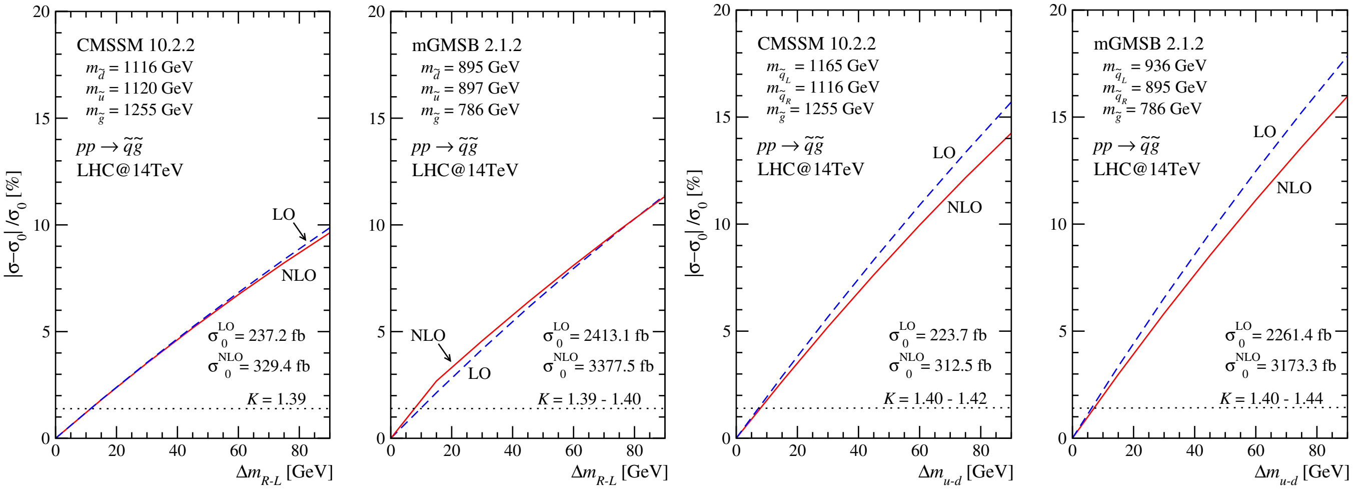

FIG. 9 (color online). Cross sections for squark-gluino production $pp \to \tilde{q}\,\tilde{g}$ ($\tilde{q} = \tilde{u}_{L,R}$, $\tilde{d}_{L,R}$) as a function of mass splittings, within the same setup as in Fig. 6.

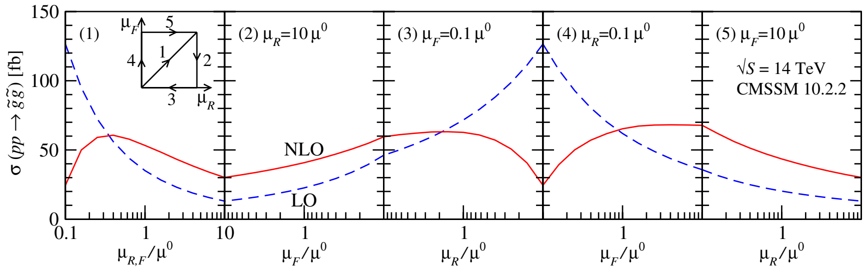

FIG. 10 (color online). Renormalization and factorization scale dependence for gluino pair production. The plot traces a contour in the μ_R-μ_F plane in the range $\mu = (0.1\text{–}10) \times \mu^0$ with $\mu^0 = m_{\tilde{g}}$. All parameters are the same as for Fig. 4, with $m_{\tilde{g}} = 1255$ GeV.

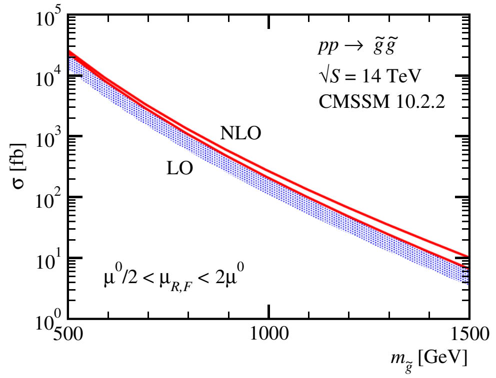

FIG. 11 (color online). Cross sections for $\sigma(pp \to \tilde{g}\,\tilde{g})$ as a function of the gluino mass $m_{\tilde{g}}$. The band corresponds to a scale variation $\mu^0/2 < \mu_{R,F} < 2\mu^0$ with $\mu^0 = m_{\tilde{g}}$. The MSSM parameters are given by the CMSSM 10.2.2 benchmark point. The squark and gluino masses we vary in parallel, just like in Fig. 2.

gluino mass. It reflects a reduction of the theoretical uncertainties from $\mathcal{O}(70\%)$ at LO down to $\mathcal{O}(30\%)$ at NLO. In spite of the large K factor triggered by the LO parton densities the two bands nicely overlap.

From the discussions of the squark pair and squark-gluino channels we expect the effect of the nondegenerate squark spectrum on gluino pair production to be small. The leading phase space effects which appear as factorizing corrections in the other production channels are absent for gluino pairs. Only the LO squark mass dependence through the t-channel exchange diagram and the specific NLO loop effects remain. For the mGMSB 2.1.2 benchmark point we compute these effects and find a deviation of roughly 2% when we allow for a right-left mass splitting of 100 GeV.

III. DISTRIBUTIONS

All through Sec. II we have limited our discussions to total cross sections. This corresponds to the way higher-order corrections to new physics processes are usually implemented in experimental analyses. Event simulation including all differential cross section is performed by any of the parton shower Monte Carlos. Because the hard process scale is given by the heavy particle masses it is usually well above the typical jet momenta required by inclusive searches. This means that the parton shower approximation is justified [5] while the total cross sections have to be corrected for higher-order effects. In the original PROSPINO calculations transverse momentum and rapidity distributions for the heavy squarks and gluinos were studied [9–11], indicating that no large NLO effects should be expected. MADGOLEM allows us to include a comprehensive study of distributions in this paper.

A. Fixed order vs jet merging

To make quantitative statements beyond total cross sections we use MADGOLEM to compute NLO distributions for different squark and gluino final states. Because the MADGOLEM output is weighted events for the regularized virtual and real emission channels we can plot any distribution which makes sense in perturbative QCD. The only limitation is the validity of fixed-order QCD, reaching its limitations for example when studying the jet recoil against the heavy squark-gluino system.

For comparison we do not rely on the usual parton shower simulations, but employ more modern matrix element and parton shower merging [34–36]. We generate tree-level matrix element events with zero, one, or two hard jets with the help of MADGRAPH5 [21] and combine them with each other and with the PYTHIA [37] shower using the MLM (Michellangelo Mangano) procedure [34] as implemented in MADGRAPH. When defining the hard matrix element corrections we follow three different approaches. First, we include up to one additional hard gluon in the matrix elements. This automatically excludes all topologies which could lead to on-shell divergences. Second, we instead allow for two additional hard gluons in the matrix elements. As before, we avoid any issues with on-shell singularities. Finally, we generate samples with one additional quark or gluon. In this case, on-shell divergences will appear just like for the real emission contributing to the NLO rate. These singularities we remove using the numerical prescription implemented in MADGRAPH [21]. It subtracts all events with phase space configurations close to the on-shell poles. While this subtraction is not equivalent to the consistent PROSPINO scheme and does not have a well-defined zero-width limit we have checked that it gives

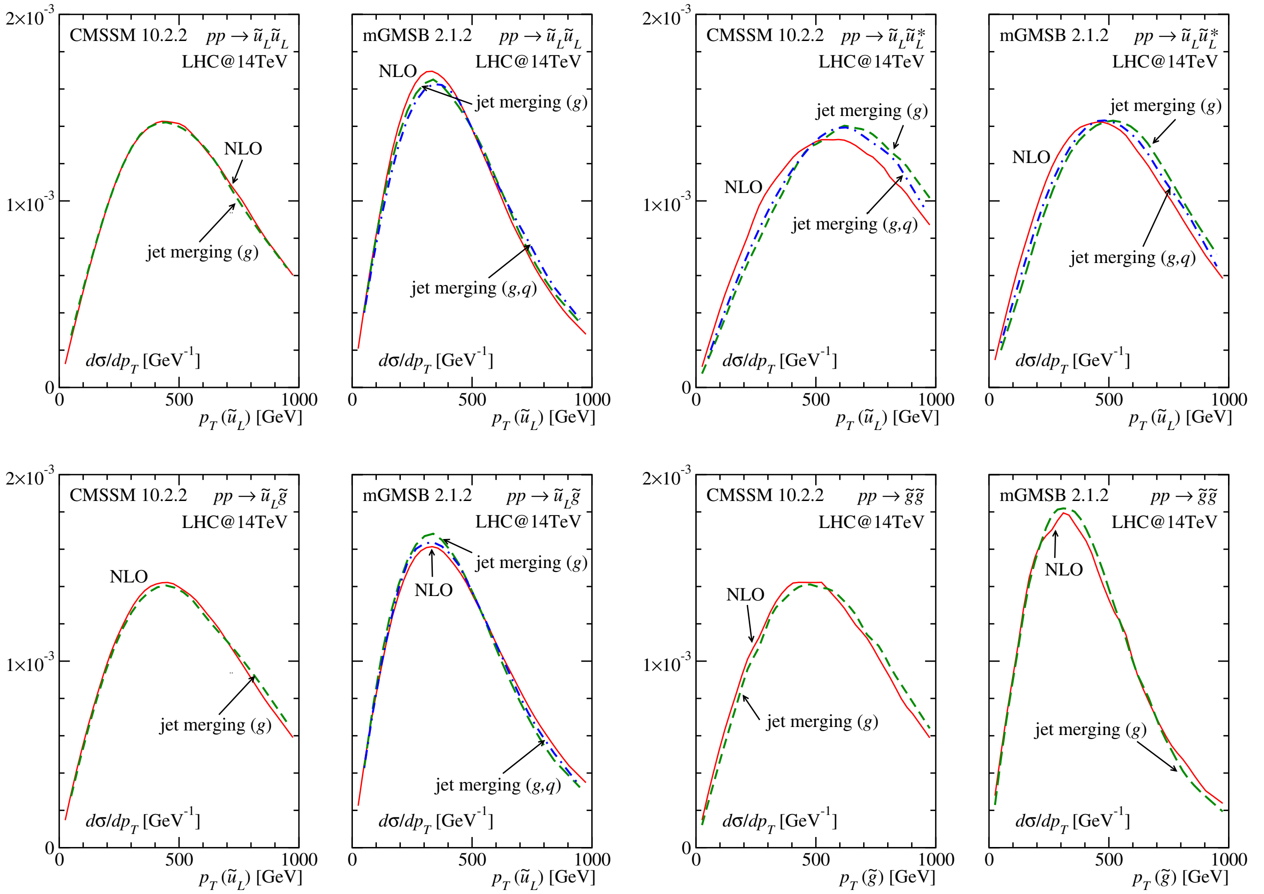

FIG. 12 (color online). Normalized transverse momentum distributions for different processes for the benchmark points CMSSM 10.2.2 and mGMSB 2.1.2. We compare NLO predictions to LO jet merging [34] with three different setups: up to one hard gluon, up to two hard gluons, up to one hard quark or gluon jet. The latter two we only display when differences are visible.

numerically similar results as long as we only compare normalized distributions.

Our results for the transverse momentum distributions of squarks and gluinos we present in Fig. 12. We focus on the CMSSM 10.2.2 and mGMSB 2.1.2 benchmark points as representative MSSM scenarios. They exemplify both possible squark-gluino mass hierarchies. As described above, we show the NLO predictions and the one-gluon merged results. Comparing different jet merging setups we confirm that adding a second hard gluon does not change our results beyond numerical precision, so we do not show it separately. This is an effect of the large hard scale in the process which renders the parton shower for the second radiated gluon an excellent approximation. We only show results allowing for one additional quark or gluon jet when the curves are visibly different from the one-gluon case. The general agreement of all three merging results shows that once the double counting from the on-shell states is removed the bulk of the NLO real emission comes from gluons. Moreover, this gluon radiation is well described by the PYTHIA parton shower, as long as the produced particles are heavy [5]. However, once an experimental analysis becomes particularly sensitive to the jet recoil it might pay off to check the parton shower results with a merged sample [6,38].

The comparison with the NLO prediction shows that the usual assumption about the stability of the main distributions is indeed correct. The normalized distributions from the fixed-order NLO calculation and from multijet merging agree very well. As alluded to above, the multijet merging predictions in turn agree well with the parton shower. In spite of the remarkable agreement between both descriptions, some mild departures are visible. We can essentially understand them as a fingerprint of the extra recoil jets involved in the matched samples. For example, in some cases the jet merging predictions become slightly harder than the NLO results because they take into account a second radiated jet. On the other hand, the squarks and gluinos we are studying are so heavy that it is unlikely that jet radiation makes a big difference to them.

In MADGOLEM the generation of any kind of fixed-order distributions, such as those displayed in Fig. 12, is completely automated. This constitutes a substantial improvement for precision beyond the standard model predictions. Distributions can be computed for a single kinematic variable, but also two-dimensionally. For example, we show

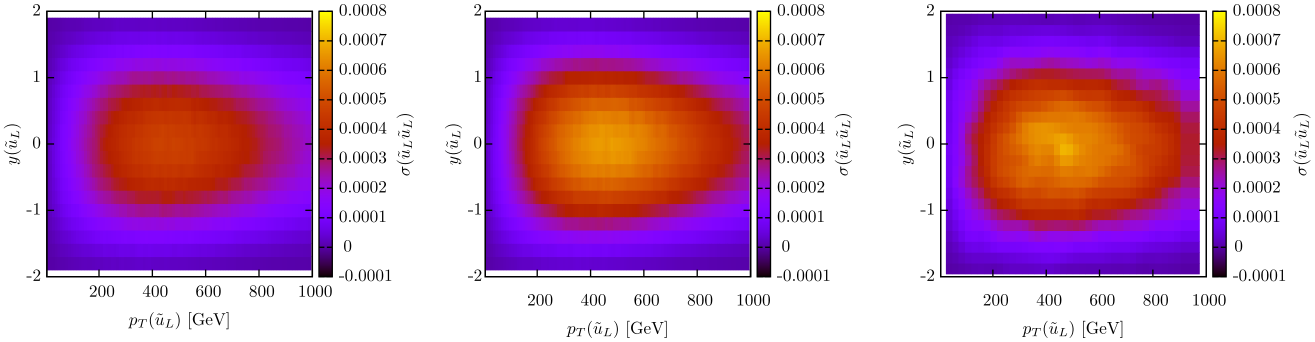

FIG. 13 (color online). Two-dimensional distributions for squark pair production $pp \rightarrow \tilde{u}_L\tilde{u}_L$ at $\sqrt{S} = 14$ TeV as contour plots in the $p_T(\tilde{u}_L)$-$y(\tilde{u}_L)$ plane. The different panels show the results from LO (left), NLO (center), and jet merging (right). While the LO result is shown to scale the two right histograms are normalized to unity. We use the CMSSM 10.2.2 parameters.

the NLO phase space dependence on the transverse momentum and the rapidity of one final-state particle in Fig. 13. The three panels give LO, NLO, and merged predictions for squark pair production $pp \rightarrow \tilde{u}_L\tilde{u}_L$. The NLO and the merging histograms are normalized to unity, while the LO distribution is shown to scale. As expected, we do not find any kind of significant difference between the NLO and the jet merging results or any correlations between the rapidity and transverse momentum.

B. Scale uncertainties

The stabilization of the (unphysical) dependence with respect to the choice of the renormalization and factorization scales is a most prominent feature of NLO calculations. These improvements, which we have already analyzed for the total cross section, we reexamine now for the distributions. Again, we study squark pair production $pp \rightarrow \tilde{u}_L\tilde{u}_L$. In Fig. 14 we present the squark transverse momentum and rapidity distributions.

We first overlay the normalized distributions from the fixed-order NLO calculation (solid, red line) with the central scale choice and the jet merging results (dashed, green line) for the CMSSM 10.2.2 and mGMSB 2.1.2 parameter points. For the NLO curve we compute the envelope varying the renormalization and factorization scales between $\mu^0/2$ and $2\mu^0$, keeping the normalization relative to the central scale choice. This should give a realistic estimate of the theoretical uncertainty.

Two differences we show separately: first, the yellow (light) histogram shows the difference $d\sigma/dp_T(\mu^0/2) - d\sigma/dp_T(2\mu^0)$. It indicates a theoretical uncertainty of $\mathcal{O}(10\%)$ on the distribution, with no obvious caveats. In addition, we show the difference between the central NLO prediction and MLM multijet merging $d\sigma^{\mathrm{MLM}}/dp_T - d\sigma^{\mathrm{NLO}}/dp_T$ point-by-point in the purple (dark) histogram. Both comparisons we repeat for the squark rapidity distributions. We see that when it comes to normalized distributions the NLO and MLM multijet merging predictions

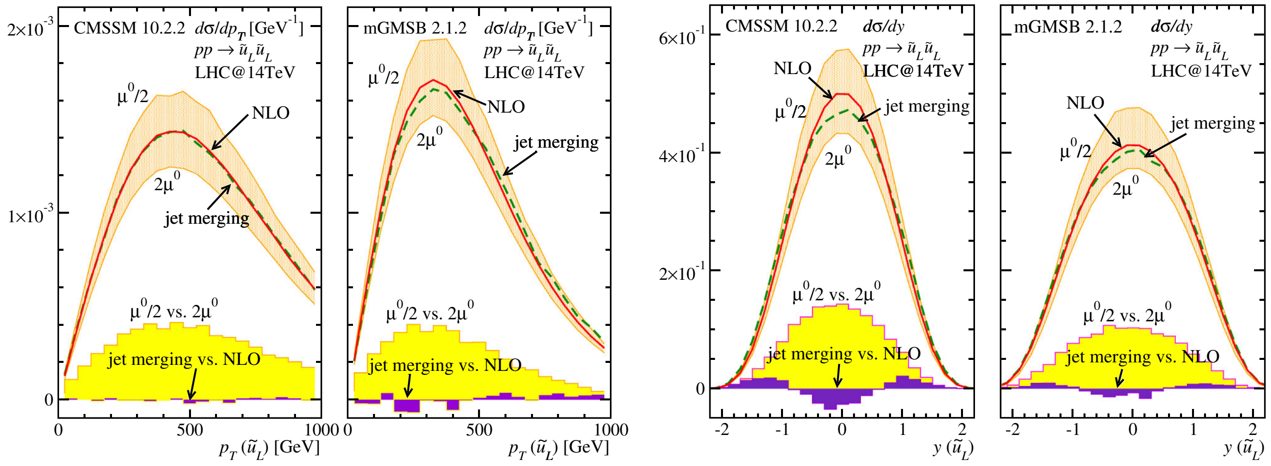

FIG. 14 (color online). Distributions for squark pair production $pp \rightarrow \tilde{u}_L\tilde{u}_L$ as a function of the squark transverse momentum (left) and rapidity (right). The curves for the central scales we normalize to unity. The scale uncertainty curves we normalize to the same central value. The yellow area shows the scale uncertainty, e.g., $d\sigma/dp_T(\mu^0/2) - d\sigma/dp_T(2\mu^0)$, compared to the purple area giving $d\sigma^{\mathrm{MLM}}/dp_T - d\sigma^{\mathrm{NLO}}/dp_T$. We examine the benchmark points CMSSM 10.2.2 and mGMSB 2.1.2.

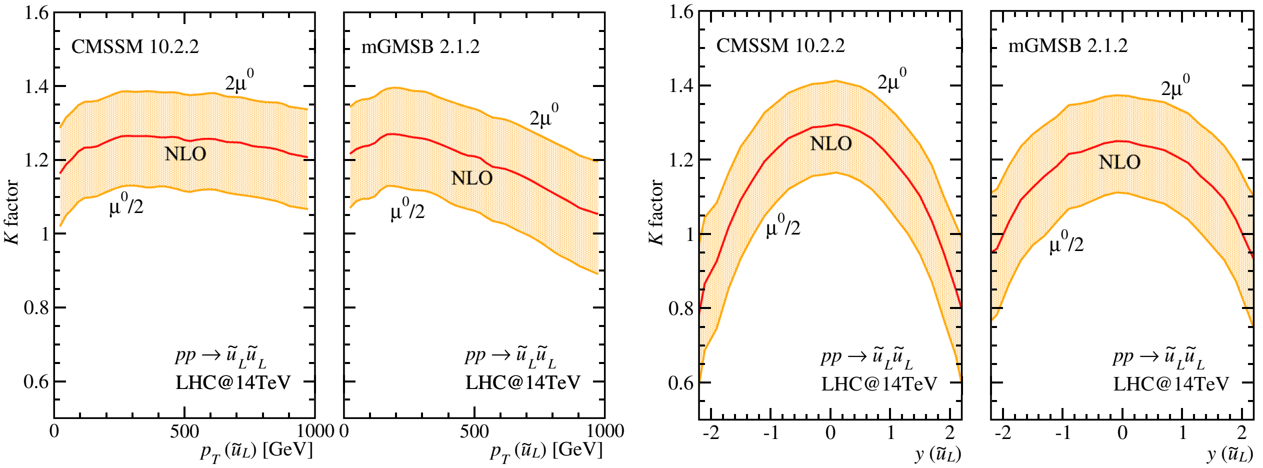

FIG. 15 (color online). K factor as a function of $p_T(\tilde{u}_L)$ and $y(\tilde{u}_L)$ for squark production $pp \to \tilde{u}_L \tilde{u}_L$. The band shows a scale variation $\mu^0/2 < \mu < 2\mu^0$. All MSSM parameters we fix to CMSSM 10.2.2 and mGMSB 2.1.2.

are in excellent agreement, for example, compared to the sizable NLO scale dependence.

A complementary viewpoint in terms of phase space dependent K factors we display in Fig. 15. The NLO histograms using central scales μ^0 are supplemented by a band showing a simultaneous renormalization and factorization scale dependence at NLO. We confirm that the K factors remain stable and relatively constant for the transverse momentum and the central rapidity regime. From the above discussion we know that the slight change in the K factor over the entire phase space should correspond to distributions computed using multijet merging. This result we interpret as a strong argument in favor of the conventional procedure, where a global K factor or event reweighting to NLO is applied to kinematic distributions generated via multijet merging.

C. Nondegenerate squarks

In Sec. II we discuss the effect of a general squark mass spectrum on the different LHC production rates and find that it largely factorizes from the NLO corrections; i.e., the K factors only change at the percent level. The impact of general squark mass spectra becomes much more apparent at the distribution level. In Fig. 16 we display the squark transverse momentum and rapidity distributions. We single out one particular production channel, $pp \to \tilde{u}_L \tilde{g}$, and examine the following representative situations: (i) mass-degenerate squarks, with $m_{\tilde{q}} = 800$ GeV; (ii) a right-left splitting $\Delta m_{R-L} = 200$ GeV between the right-handed and left-handed squarks; and (iii) a similar down-up splitting $\Delta m_{d-u} = 200$ GeV. The remaining MSSM parameters we anchor as in the mGMSB 2.1.2 benchmark point defined in Table I. Most importantly,

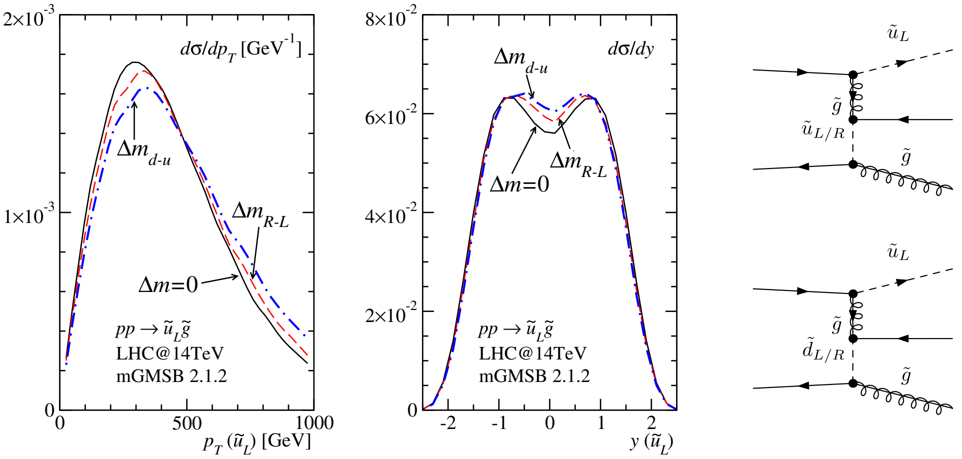

FIG. 16 (color online). Normalized transverse momentum (left) and rapidity distributions (right) for squark-gluino production $pp \to \tilde{u}_L \tilde{g}$. We assume (i) mass-degenerate squarks with $m_{\tilde{q}} = 800$ GeV; (ii) a common mass splitting, $\Delta m_{R-L} = 200$ GeV; (iii) a common mass splitting, $\Delta m_{d-u} = 200$ GeV. The central MSSM parameters we fix as in mGMSB 2.1.2 benchmark. The Feynman diagrams to the right describe the squark-gluino fusion mechanism responsible for the significant differences.

we keep the final-state mass constant, so the differences between these three scenarios decouple from the leading phase space effects and instead constitute a genuine NLO reflection.

The finite mass splitting between squarks induces a shift in the kinematic distributions in the direction of slightly harder and more central final-state squarks. We can trace this back to the real emission corrections shown in Fig. 16. They describe a fusion mechanism where the bulk contribution arises from internal squark and gluino propagators at very small virtuality, i.e., when these particles are almost on-shell. As a result, they become particularly sensitive to variations of the squark masses, even if the final-state squarks masses remain unchanged.

As we can see in Fig. 16 the effect of an $\mathcal{O}(20\%)$ mass splitting between up-type and down-type squarks saturates the NLO uncertainty on the transverse momentum distributions. Of course, the squark mass spectrum is not a source of theory uncertainty which could be captured by the scale dependence. Therefore, it might be useful to estimate its effect on LHC analyses independently.

IV. SUMMARY

MADGOLEM is a novel approach to the automated computation of total cross sections and distributions for new heavy particles to next-to-leading order. It can be used as an add-on to MADGRAPH, making use of its interfaces to new models as well as to the event generation. In this paper we present a comprehensive overview of supersymmetric particle production together with many details of the MADGOLEM implementation. While MADGOLEM is not fully public yet, a fully functional test version can be obtained from the authors upon request.

In our application to squark and gluino production we reproduce all relevant PROSPINO results and extend currently available studies in several ways:

(i) We evaluate NLO corrections to total rates for a completely general supersymmetric mass spectrum. For moderate mass splittings the leading effects of nondegenerate squarks factorize from the LO results, while the effect on K factors stays at the level of a few percent.

(ii) Instead of identifying the factorization and renormalization scales in the estimate of the theoretical uncertainty we vary both scales independently. For heavy strongly interacting new particles the envelope of all possible scales agrees with a simultaneous scale variation.

(iii) Squark and gluino distributions including the full NLO corrections and based on multijet merging agree very well within the NLO error bands.

(iv) The effect of nondegenerate spectra on the squark and gluino distributions is clearly visible and can exceed the perturbative uncertainty already at moderate mass splittings.

(v) The composition of the NLO corrections from different classes of diagrams and with it the dependence of the K factors on the mass of the produced particles is significantly different for quark-antiquark vs gluonic initial states, i.e., moving from Tevatron to LHC.

In addition to these specific conclusions we emphasize that with MADGOLEM this kind of study can be easily repeated for any kind of heavy new particles at the LHC. In the light of the available LHC results this might be useful not only for general simplified models but also for specific models outside the usual MSSM model and parameter space. For this purpose we include an Appendix A which provides all necessary information on the infrared dipole subtraction as well as on a proper on-shell subtraction as implemented in MADGOLEM.

ACKNOWLEDGMENTS

We would like to thank Thomas Binoth, who started this project with us and unfortunately cannot see its completion. The work presented here has been in part supported by the Concerted Research action “Supersymmetric Models and Their Signatures at the Large Hadron Collider” and the Research Council of the Vrije Universiteit Brussel and by the Belgian Federal Science Policy Office through the Interuniversity Attraction Pole IAP VI/11. D. G. acknowledges support by the International Max Planck Research School for Precision Tests of Fundamental Symmetries.

APPENDIX A: SUPERSYMMETRIC DIPOLES

In this Appendix we present the unintegrated and integrated dipoles required for SUSY-QCD calculations [26] including a phase space constraint [29]. They are implemented as an independent add-on to the MADDIPOLE package [39] and are part of the automated MADGOLEM framework.

There exist two major approaches to remove soft and collinear singularities: phase space slicing and phase space subtraction [36]. A simple toy example captures their main features and highlights the role of a FKS-like phase space constraint [29]. Let us consider the dimensionally regularized integral $\int_0^1 dx f(x)/x^{1-\epsilon}$ with $\epsilon > 0$. Phase space slicing based on a small parameter α yields

$$\begin{aligned}\int_0^1 dx \frac{f(x)}{x^{1-\epsilon}} &= \int_\alpha^1 dx \frac{f(x)}{x^{1-\epsilon}} + \int_0^\alpha dx \frac{f(0)}{x^{1-\epsilon}} + \mathcal{O}(\alpha)\\ &= \int_\alpha^1 dx \frac{f(x)}{x} + \frac{f(0)}{\epsilon} + f(0)\log\alpha + \mathcal{O}(\alpha;\epsilon).\end{aligned} \tag{A1}$$

It requires a choice of small enough α to reach a numerical plateau. A numerically more stable approach is phase space subtraction, where the same integral becomes

$$\begin{aligned}\int_0^1 dx\frac{f(x)}{x^{1-\epsilon}} &= \int_0^1 dx\frac{f(x)-f(0)\Theta(x\le\alpha)}{x^{1-\epsilon}} + \int_0^\alpha dx\frac{f(0)}{x^{1-\epsilon}} \\ &= \int_0^1 dx\frac{f(x)-f(0)\Theta(x\le\alpha)}{x} + \frac{f(0)}{\epsilon} \\ &\quad + f(0)\log\alpha + \mathcal{O}(\epsilon). \qquad \text{(A2)}\end{aligned}$$

Here the divergence is subtracted locally and the final result no longer depends on α. The logarithmic α dependence is exactly canceled in the total result. This feature we can turn into a sensitive numerical test when varying $0 < \alpha \le 1$. For small values of α we only need to evaluate part of the integrand of Eq. (A2), which speeds up the calculation.

The toy model of Eq. (A2) carries the essence of the Catani-Seymour subtraction method. Real emission of quarks and gluons ($d\sigma^{\text{real}}$) leads to IR divergences after an integration over the emission phase space. Its regularization relies on a local subtraction term ($d\sigma^{\text{A}}$) which reflects the universality of the soft and collinear limits. The divergence cancels over the same n-particle phase space,

$$\begin{aligned}\delta\sigma^{\text{NLO}} &= \int_{n+1}(d\sigma^{\text{real}}_{\epsilon=0} - d\sigma^{\text{A}}_{\alpha,\epsilon=0}) + \int_n (d\sigma^{\text{virtual}} \\ &\quad + d\sigma^{\text{collinear}} + \int_1 d\sigma^{\text{A}}_{\alpha})_{\epsilon=0}. \qquad \text{(A3)}\end{aligned}$$

Below, we present the unintegrated dipoles $d\sigma^{\text{A}}_{\alpha}$ as well as the integrated dipoles $\int_1 d\sigma^{\text{A}}_{\alpha}$ including their α dependence. They are crucial for SUSY-QCD processes or other NLO QCD predictions beyond the standard model. Our extended set of massive Catani-Seymour dipoles with explicit α dependence has several practical advantages:

- Tuning α we reduce the subtraction phase space and hence the number of events for which the real emission matrix element and the subtraction fall into different bins: the so-called *binning problem*.
- Choosing $\alpha < 1$ we evaluate the subtraction terms only in the phase space region where they matter, i.e., close to the IR divergences.
- Our final result should not depend on α. This serves as a test for example of the adequate coverage of all the singularities or the relative normalization of the two-particle and three-particle phase space.

In the MSSM gluino and squark interactions induced by the covariant derivatives $\bar{\tilde{g}}\not{D}\tilde{g}$, $|D_\mu\tilde{q}|^2$ give rise to new IR divergences which are absent in the standard model. The emission of a soft gluon from these particles requires new final-final dipoles $D_{ij,k}$ and final-initial dipoles D^a_{ij}. Initial-initial and initial-final configurations can also have a squark or gluino as spectator, but the dipole only carries information about the mass of the colored spectator, not about its spin. This means we can simply use the massive standard model dipoles [26] with an extra SUSY particle in the final state. To make this Appendix most useful we will firmly stick to the conventions of Ref. [26].

We start with a collection of formulas for final-final dipoles. The expression for the unintegrated dipole is given by

$$\begin{aligned}D_{ij,k} &= -\frac{1}{2p_i\cdot p_j} \\ &\quad \times\left\langle \ldots,\widetilde{ij},\ldots,\tilde{k},\ldots\left|\frac{\mathbf{T}_k\mathbf{T}_{ij}}{\mathbf{T}^2_{ij}}\mathbf{V}_{ij,k}\right|\ldots,\widetilde{ij},\ldots,\tilde{k},\ldots\right\rangle, \\ &\qquad \text{(A4)}\end{aligned}$$

where $|\ldots,\widetilde{ij},\ldots,\tilde{k},\ldots\rangle$ represents the amplitude for the factorized born process, which in the special case of the SUSY dipoles is made by the removal of the gluon from the diagonal splitting $\tilde{q}(p_{ij})\to\tilde{q}(p_j)g(p_i)$. The color matrix $\mathbf{T}_k\mathbf{T}_{ij}/\mathbf{T}^2_{ij}$ acts on the born amplitude $|\ldots,\widetilde{ij},\ldots,\tilde{k},\ldots\rangle$ giving the proper color factor.

To compute the integrated dipoles we integrate over the one-particle phase space $[dp_i(\tilde{p}_{ij},\tilde{p}_k)]$ with the spin average matrices $\langle\mathbf{V}_{ij,k}\rangle$, according to Eq. (5.22) of Ref. [26]:

$$\begin{aligned}&\int[dp_i(\tilde{p}_{ij},\tilde{p}_k)]\frac{1}{(p_i+p_j)^2-m^2_{ij}}\langle\mathbf{V}_{ij,k}\rangle \\ &\quad \equiv \frac{\alpha_s}{2\pi}\frac{1}{\Gamma(1-\epsilon)}\left(\frac{4\pi\mu^2}{Q^2}\right)^\epsilon I_{ij,k}(\epsilon), \qquad \text{(A5)}\end{aligned}$$

where the squark dipole function, $\langle s|\mathbf{V}_{\mathbf{g}\tilde{\mathbf{q}},\mathbf{k}}|s'\rangle$, is given by Eq. (C1) of the same reference,

$$\begin{aligned}\frac{\langle s|\mathbf{V}_{g\tilde{q},k}|s'\rangle}{8\pi\mu^{2\epsilon}\alpha_s C_F} &= \left[\frac{2}{1-\tilde{z}_j(1-y_{ij,k})} - \frac{\tilde{v}_{ij,k}}{v_{ij,k}}\left(2+\frac{m^2_{\tilde{q}}}{p_ip_j}\right)\right]\delta_{ss'} \\ &= \frac{\langle\mathbf{V}_{g\tilde{q},k}\rangle\delta_{ss'}}{8\pi\mu^{2\epsilon}\alpha_s C_F}. \qquad \text{(A6)}\end{aligned}$$

Compared to a massive quark the squark structure is much simpler. This is because for scalars the labels s and s' are merely tagging the helicity of the associated quark partners without any effect on the squark splitting.

The integrated dipole $I_{g\tilde{q},k}$ we decompose into a soft or eikonal part I^{eik} and a collinear integral $I^{\text{coll}}_{g\tilde{q},k}$ evaluated in $4-2\epsilon$ dimensions,

$$\begin{aligned}I_{g\tilde{q},k}(\mu_{\tilde{q}},\mu_k;\epsilon) &= C_F[2I^{\text{eik}}(\mu_{\tilde{q}},\mu_k;\epsilon) + I^{\text{coll}}_{g\tilde{q},k}(\mu_{\tilde{q}},\mu_k;\epsilon)], \\ \tilde{v}_{g\tilde{q},k}I^{\text{eik}} &= \frac{1}{2\epsilon}\log\rho - \log\rho\log(1-(\mu_{\tilde{q}}+\mu_k)^2) \\ &\quad -\frac{1}{2}\log^2\rho_{\tilde{q}} - \frac{1}{2}\log^2\rho_k + \zeta_2 + 2\text{Li}_2(-\rho) \\ &\quad - 2\text{Li}_2(1-\rho) - \frac{1}{2}\text{Li}_2(1-\rho^2_{\tilde{q}}) \\ &\quad -\frac{1}{2}\text{Li}_2(1-\rho^2_k), \\ I^{\text{coll}}_{g\tilde{q},k} &= \frac{2}{\epsilon} - \frac{1}{\epsilon\mu^{2\epsilon}_{\tilde{q}}} - \frac{2}{\mu^{2\epsilon}_{\tilde{q}}} + 6 - 2\log((1-\mu_k)^2 \\ &\quad - \mu^2_{\tilde{q}}) + \frac{4\mu_k(\mu_k-1)}{1-\mu^2_{\tilde{q}}-\mu^2_k}. \qquad \text{(A7)}\end{aligned}$$

The rescaled masses μ_n and the variables ρ and ρ_n associated with the splitting $\tilde{ij}\to ij$ and the spectator k

are defined in terms of the final-state momenta p_i, p_j, and p_k as

$$\mu_n = \frac{m_n}{\sqrt{(p_i + p_j + p_k)^2}},$$

$$\rho = \sqrt{\frac{1 - \tilde{v}_{ij,k}}{1 + \tilde{v}_{ij,k}}}, \quad \text{with} \quad \tilde{v}_{ij,k} = \frac{\sqrt{\lambda(1, \mu_{ij}^2, \mu_k^2)}}{1 - \mu_{ij}^2 - \mu_k^2},$$

$$\rho_n(\mu_j, \mu_k) = \sqrt{\frac{1 - \tilde{v}_{ij,k} + 2\mu_n^2/(1 - \mu_j^2 - \mu_k^2)}{1 + \tilde{v}_{ij,k} + 2\mu_n^2/(1 - \mu_j^2 - \mu_k^2)}} \quad (n = j, k), \tag{A8}$$

with λ denoting the Källen function

$$\lambda(x, y, z) = x^2 + y^2 + z^2 - 2xy - 2xz - 2yz. \tag{A9}$$

The splitting kinematics we describe using

$$\begin{aligned} \tilde{z}_j &= 1 - \frac{p_i p_k}{p_i p_k + p_j p_k} \quad \text{and} \\ y_{ij,k} &= \frac{p_i p_j}{p_i p_j + p_i p_k + p_j p_k} > y_+ \\ &= 1 - \frac{2\mu_k(1 - \mu_k)}{1 - \mu_i^2 - \mu_j^2 - \mu_k^2}. \end{aligned} \tag{A10}$$

Just like for massive quarks there is no collinear singularity, so the most divergent term in the $I_{g\tilde{q},k}(\epsilon)$ is a single $1/\epsilon$ pole.

To include the phase space parameter α into the massive squark dipole we limit the dipole function to small values of $y_{ij,k}/y_+$:

$$D_{g\tilde{q},k} \to D_{g\tilde{q},k}\Theta\left(\frac{y_{ij,k}}{y_+} < \alpha\right), \qquad \alpha \epsilon (0, 1]. \tag{A11}$$

For the integrated dipole $I_{g\tilde{q},k}(\epsilon)$ we start from Eq. (A7) and subtract the finite term including the same kinematic condition as Eq. (A11):

$$\begin{aligned} I_{g\tilde{q},k}(\epsilon, \alpha) &= I_{g\tilde{q},k}(\epsilon) + \Delta I_{g\tilde{q},k}(\alpha) \\ &= I_{g\tilde{q},k}(\epsilon) - \frac{2\pi}{\alpha_s}\int [dp_g(\tilde{p}_{g\tilde{q}}, \tilde{p}_k)] \\ &\quad \times \frac{\langle \mathbf{V}_{g\tilde{q},k}\rangle}{2p_g p_{\tilde{q}}}\Theta\left(\frac{y_{g\tilde{q},k}}{y^+} > \alpha\right). \end{aligned} \tag{A12}$$

The finite part we can evaluate in four dimensions, because by definition there exists no divergence in the region $y_{g\tilde{q},k}/y^+ > \alpha$. The eikonal part $2/[1 - \tilde{z}_{\tilde{q}}(1 - y_{g\tilde{q},k})]$ is the same for $\langle s|\mathbf{V}_{gQ,k}|s'\rangle$ and $\langle s|\mathbf{V}_{g\tilde{q},k}|s'\rangle$, so in Eq. (A12) we insert Eq. (A7) from our Appendix and Eq. (A.9) from Ref. [40],

$$\begin{aligned} \tilde{v}_{g\tilde{q},k}\Delta I^{\text{eik}}(\alpha) = {}& -\text{Li}_2\left(\frac{a + x}{a + x_+}\right) + \text{Li}_2\left(\frac{a}{a + x_+}\right) + \text{Li}_2\left(\frac{x_+ - x}{x_+ - b}\right) - \text{Li}_2\left(\frac{x_+}{x_+ - b}\right) + \text{Li}_2\left(\frac{c + x}{c + x_+}\right) - \text{Li}_2\left(\frac{c}{c + x_+}\right) \\ & + \text{Li}_2\left(\frac{x_- - x}{x_- + a}\right) - \text{Li}_2\left(\frac{x_-}{x_- + a}\right) - \text{Li}_2\left(\frac{b - x}{b - x_-}\right) + \text{Li}_2\left(\frac{b}{b - x_-}\right) - \text{Li}_2\left(\frac{x_- - x}{x_- + c}\right) + \text{Li}_2\left(\frac{x_-}{x_- + c}\right) \\ & + \text{Li}_2\left(\frac{b - x}{b + a}\right) - \text{Li}_2\left(\frac{b}{b + a}\right) - \text{Li}_2\left(\frac{c + x}{c - a}\right) + \text{Li}_2\left(\frac{c}{c - a}\right) + \log(c + x)\log\left(\frac{(a - c)(x_+ - x)}{(a + x)(c + x_+)}\right) \\ & - \log(c)\log\left(\frac{(a - c)x_+}{a(c + x_+)}\right) + \log(b - x)\log\left(\frac{(a + x)(x_- - b)}{(a + x)(x_- - x)}\right) - \log(b)\log\left(\frac{a(x_- - b)}{(a + b)x_-}\right) \\ & - \log((a + x)(b - x_+))\log(x_+ - x) + \log(a(b - x_+))\log(x_+) + \log(d)\log\left(\frac{(a + x)x_+ x_-}{a(x_+ - x)(x_- - x)}\right) \\ & + \log\left(\frac{x_- - x}{x_-}\right)\log\left(\frac{c + x_-}{a + x_-}\right) + \frac{1}{2}\log\left(\frac{a + x}{a}\right)\log(a(a + x)(a + x_+)^2), \end{aligned} \tag{A13}$$

where

$$a = \frac{2\mu_k}{1 - \mu_{\tilde{q}}^2 - \mu_k^2}, \qquad b = \frac{2(1 - \mu_k)}{1 - \mu_{\tilde{q}}^2 - \mu_k^2}, \tag{A14}$$

$$c = \frac{2\mu_k(1 - \mu_k)}{1 - \mu_{\tilde{q}}^2 - \mu_k^2}, \qquad d = \frac{1}{2}(1 - \mu_{\tilde{q}}^2 - \mu_k^2), \tag{A15}$$

and

$$x_\pm = \frac{(1 - \mu_k)^2 - \mu_{\tilde{q}}^2 \pm \sqrt{\lambda(1, \mu_{\tilde{q}}^2, \mu_k^2)}}{1 - \mu_{\tilde{q}}^2 - \mu_k^2}. \tag{A16}$$

The collinear part is different for squarks, so we supplement its form in Eq. (A7) by

$$\Delta I_{g\tilde{q},k}^{\text{coll}}(\alpha) = -\frac{C_F}{2\pi^2}\left[\frac{(1 - \mu_k)^2 - \mu_{\tilde{q}}^2}{1 - \mu_{\tilde{q}}^2 - \mu_k^2}(1 - \alpha) + \log\alpha\right]. \tag{A17}$$

Following the same logic we tackle the final-initial dipoles. The final-initial dipole function is given by Eq. (C.3) of Ref. [26],

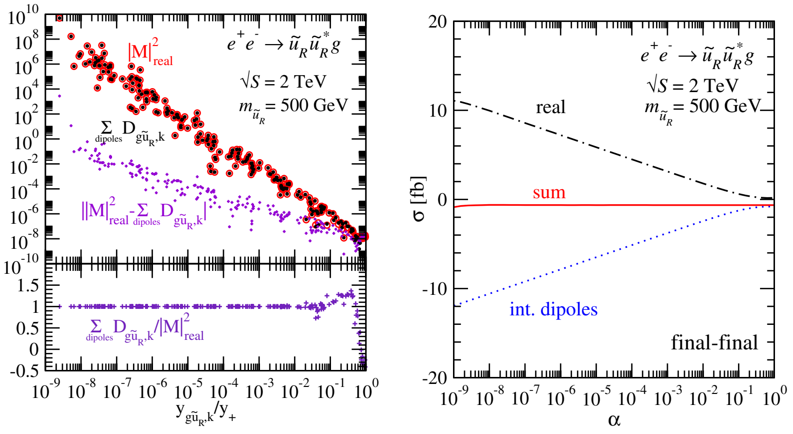

FIG. 17 (color online). Left: real emission matrix element (red circles) and the dipole subtraction (black crosses inside) towards the soft limit $y_{g\tilde q,k} \to 0$. Right: α dependence for final-final squark dipoles.

$$\langle \mathbf{V}^a_{g\tilde q}\rangle = 8\pi\mu^{2\epsilon}\alpha_s C_F\left(\frac{2}{2-x_{g\tilde q,a}-\tilde z_{\tilde q}} - 2 - \frac{m^2_{\tilde q}}{p_g p_{\tilde q}}\right). \tag{A18}$$

The integrated dipole function $I^a_{g\tilde q}$ becomes

$$\begin{aligned} I^a_{g\tilde q}(x;\epsilon) = C_F[(J^a_{g\tilde q}(x,\mu_{\tilde q}))_+ + \delta(1-x)(J^{a;S}_{g\tilde q}(\mu_{\tilde q};\epsilon) \\ + J^{a;NS}_{g\tilde q}(\mu_{\tilde q}))] + \mathcal{O}(\epsilon), \end{aligned} \tag{A19}$$

with the three contributions $I^a_{g\tilde q}$:

$$\begin{aligned} [J^a_{g\tilde q}(x,\mu_{\tilde q})]_+ &= -2\left(\frac{1+\log(1-x+\mu^2_{\tilde q})}{1-x}\right)_+ \\ &\quad + \left(\frac{2}{1-x}\right)_+ \log(2+\mu^2_{\tilde q}-x), \\ J^{a;S}_{g\tilde q}(\mu_\sigma;\epsilon) &= \frac{1}{\epsilon^2} - \frac{\pi^2}{3} - \frac{1}{\mu^{2\epsilon}_{\tilde q}}\left(\frac{1}{\epsilon^2}+\frac{1}{\epsilon}+\frac{\pi^2}{6}+2\right) \\ &\quad - \frac{\log(1+\mu^2_{\tilde q})}{\epsilon} + \frac{2}{\epsilon} + 4 - \frac{\pi^2}{6}, \\ J^{a;NS}_{g\tilde q}(\mu_{\tilde q}) &= \frac{\pi^2}{3} - 2\mathrm{Li}_2\left(\frac{1}{1+\mu^2_{\tilde q}}\right) - 2\mathrm{Li}_2(-\mu^2_{\tilde q}) \\ &\quad - \frac{1}{2}\log^2(1+\mu^2_{\tilde q}). \end{aligned} \tag{A20}$$

In analogy to the final-final case of Eqs. (A11) and (A12) we introduce a phase space cutoff

$$\begin{aligned} D^a_{g\tilde q} &\to D^a_{g\tilde q}\Theta(\alpha - 1 + x_{g\tilde q,a}), \\ \Delta I^a_{g\tilde q}(\alpha) &= -C_F\frac{\Theta(1-\alpha-x)}{1-x} \\ &\quad \times\left[-2+2\log\left(1+\frac{1}{1+\mu^2_{\tilde q}-x}\right)\right], \end{aligned} \tag{A21}$$

where the kinematic variable $x_{ij,a}$ is given by

$$x_{ij,a} = \frac{p_a p_i + p_a p_j - p_i p_j + \frac{m^2_{ij}-m^2_i-m^2_j}{2}}{p_a p_i + p_a p_j}. \tag{A22}$$

As an example for numerous numerical tests of our dipole implementation, we discuss soft gluon emission off the hard process $e^+e^- \to \tilde u_R \tilde u_R^*$. In the left panel of Fig. 17 we show how the dipole subtraction cancels the IR divergence locally, i.e., point-by-point. The numerical agreement of the real emission matrix element with the dipole subtraction term improves for softer gluons. In the soft limit both terms grow as $1/E_g^2$. Even though we find $|\mathcal{M}^2_{\mathrm{real}} - \sum_{\mathrm{dipoles}} D_{g\tilde q,k}| \sim 1/E_g$ the phase space factor $E_g dE_g$ cancels this dependence.

In the right panel of Fig. 17 we show the α dependence for the final-final squark dipole. Both, the real emission and the integrated dipole, depend separately on α. Their sum is numerically stable over many orders of magnitude and down to $\alpha = 10^{-9}$.

APPENDIX B: ON-SHELL SUBTRACTION

From single top production it is well known that when including NLO corrections we have to avoid double counting of diagrams which are attributed to different physics processes. As an example we consider real emission corrections to squark pair production $pp \to \tilde q\, \tilde q$: the partonic subchannels with an additional quark in the final state $qg \to \tilde q\, \tilde q\, \bar q$ display a peculiar behavior which we illustrate in Fig. 18. The diagrams (a) and (b) are part of the genuine NLO corrections to squark pair production. In contrast, the diagrams (c) and (d) can be interpreted in two ways:

$$\begin{aligned} &qg \to \tilde q \tilde g^{(*)} \to \tilde q\, \tilde q\, \bar q \qquad \text{squark pair production}, \\ &qg \to \tilde q\, \tilde g \times \mathrm{BR}(\tilde g \to \tilde q\, \bar q) \qquad \text{squark-gluino production}. \end{aligned} \tag{B1}$$

The first interpretation simply assumes NLO corrections to the hard process $pp(qg) \to \tilde q\, \tilde q$ and is generally valid for

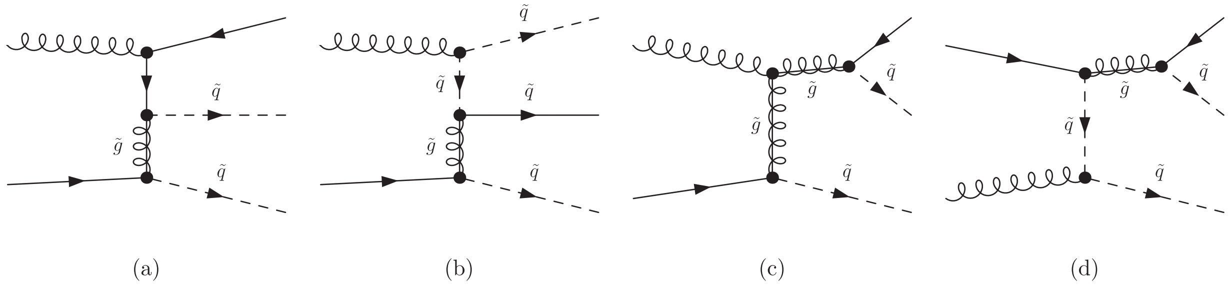

FIG. 18. Sample diagrams for the real emission corrections to squark pair production with an additional quark in the final state.

on-shell and off-shell gluinos. The second interpretation points to the LO process for $qg \to \tilde{q}\,\tilde{g}$ followed by the branching $\mathrm{BR}(\tilde{g} \to \tilde{q}\,\bar{q})$ and implicitly assumes an on-shell gluino. For a mass hierarchy $m_{\tilde{g}} > m_{\tilde{q}}$ we can therefore separate the two assignments into off-shell and on-shell gluinos. This distinction avoids double counting and is the basis of our on-shell subtraction scheme. Approaches to tackle this problem include

- (i) A slicing procedure which separates the phase space related to the on-shell emissions and removes the on-shell divergence by requiring $|\sqrt{s_{\tilde{q}\,\bar{q}}} - m_{\tilde{g}}| > \delta$ [41]. Phase space methods of this kind do not offer a cancellation of the δ dependence and do not act locally in phase space. Moreover, as a pure phase space approach it does not allow for a proper separation into finite, on-shell, and interference contributions which is crucial for a reliable rate prediction.
- (ii) Diagram removal where the resonant diagrams are removed by hand. In lucky cases this method might work in the limit $\Gamma/m \ll 1$ [42], but it ignores any kind of interference contributions which do not actually have to vanish in narrow-width limit. This scheme is theoretically poorly motivated in many ways.
- (iii) Local on-shell subtraction in the so-called PROSPINO scheme [11,27] which under the name "diagram subtraction" is also used in the single top computation of MC@NLO. This method is used in MADGOLEM.

To define the on-shell subtraction we split the contributions of the matrix element in two parts: the first piece concerns the resonant diagrams (c) and (d) and is denoted as $\mathcal{M}_{\mathrm{res}}$, while the second piece represents the nonresonant (remnant) diagrams (a) and (b) as $\mathcal{M}_{\mathrm{rem}}$. Note that this separation is defined at the amplitude level and not based on the amplitude squared. The full matrix element squared becomes

$$|\mathcal{M}|^2 = |\mathcal{M}_{\mathrm{res}}|^2 + 2\,\mathrm{Re}(\mathcal{M}^*_{\mathrm{res}}\mathcal{M}_{\mathrm{rem}}) + |\mathcal{M}_{\mathrm{rem}}|^2. \tag{B2}$$

The divergent propagator in $\mathcal{M}_{\mathrm{res}}$ we regularize as a Breit-Wigner propagator

$$\frac{1}{p_{ij}^2 - m_{ij}^2} \to \frac{1}{p_{ij}^2 - m_{ij}^2 + i m_{ij}\Gamma_{ij}}, \tag{B3}$$

where m_{ij} is the mass of the mother particle in the splitting $\widetilde{ij} \to ij$, as shown in Fig. 19, and Γ_{ij} is a regulator.

As explained above, a possible double counting is limited to the on-shell configuration in $|\mathcal{M}_{\mathrm{res}}|^2$. To remove it we define a local subtraction term $d\sigma^{\mathrm{OS}}$ and include it in complete analogy to the Catani-Seymour dipole subtraction Eq. (A3), such that the total cross section is given by

$$\delta\sigma^{\mathrm{NLO}} = \int_{n+1} (d\sigma^{\mathrm{real}}_{\epsilon=0} - d\sigma^{\mathrm{A}}_{\alpha,\epsilon=0} - d\sigma^{\mathrm{OS}}_{\epsilon=0}) + \int_n \left(d\sigma^{\mathrm{virtual}} + d\sigma^{\mathrm{collinear}} + \int_1 d\sigma^{\mathrm{A}}_{\alpha} \right)_{\epsilon=0}. \tag{B4}$$

The extra subtraction term $d\sigma^{\mathrm{OS}}$ is $|\mathcal{M}_{\mathrm{res}}|^2$ with its momenta remapped to the on-shell kinematics,

$$d\sigma^{\mathrm{OS}} = \Theta(\hat{S} - (m_{ij} + m_k)^2)\Theta(m_{ij} - m_i - m_j) \times \frac{\frac{1}{(p_{ij}^2 - m_{ij}^2)^2 + m_{ij}^2\Gamma_{ij}^2}}{\frac{1}{m_{ij}^2\Gamma_{ij}^2}} |\mathcal{M}_{\mathrm{res}}|^2 \Bigg|_{\mathrm{remapped}}. \tag{B5}$$

The kinematic configuration is depicted in Fig. 19. The two step functions in Eq. (B5) ensure that the partonic center-of-mass energy is sufficient to produce the intermediate on-shell particle and that it can decay on-shell into the two final-state particles. The ratio of the Breit-Wigner functions ensures that the subtraction has the same profile as the original $|\mathcal{M}_{\mathrm{res}}|^2$ over the entire phase space. In the small width limit this ratio reproduces the delta distribution which factorizes the $2 \to 3$ diagrams into $\sigma \times \mathrm{BR}$.

Note that this method works with a mathematical regulator Γ_{ij} which can be related to the physical width as in the MC@NLO implementation; alternatively we can go into the

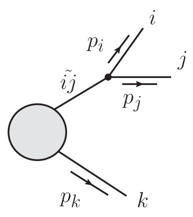

FIG. 19. Kinematic variables for the on-shell subtraction.

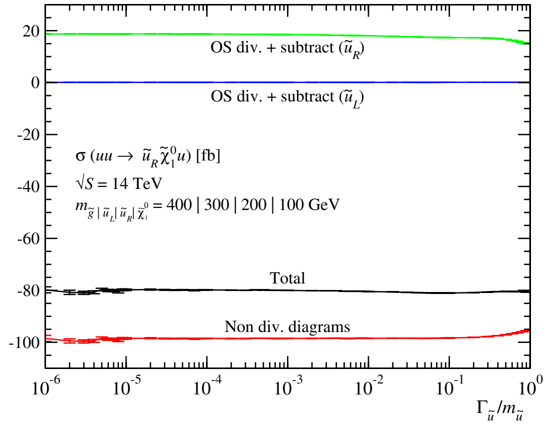

FIG. 20 (color online). NLO contributions from intermediate on-shell particles in $uu \rightarrow \tilde{u}_R \tilde{\chi}_1^0 + X$ production as a function of $\Gamma_{\tilde{u}}/m_{\tilde{u}}$. The squark width acts as a cutoff in the PROSPINO subtraction scheme [11,27]. The masses are chosen to illustrate all different resonant channels; virtual corrections are not included.

well-defined limit $\Gamma_{ij} \ll m_{ij}$ used in the original PROSPINO implementation.

In summary, this on-shell subtraction implemented in MADGOLEM exhibits several attractive features when it comes to prediction of total and differential cross sections. First, it subtracts all on-shell divergences point-by-point over the entire phase space. This means that all distributions are automatically safe. Second, it preserves gauge invariance at least in the narrow-width limit. Third, it takes into account spin correlations, because it includes the full $2 \rightarrow 3$ matrix element. Fourth, it keeps track of the interference of the resonant and nonresonant terms, $2\,\mathrm{Re}(\mathcal{M}^*_{\mathrm{res}}\mathcal{M}_{\mathrm{rem}})$, which can be numerically sizable. Finally, Fig. 20 shows that it smoothly interpolates between a finite width $\Gamma_{ij}/m_{ij} \sim 0.1$ and the narrow-width limit $\Gamma_{ij}/m_{ij} \rightarrow 0$.

APPENDIX C: ONE-LOOP AMPLITUDES

The virtual corrections module of MADGOLEM is based on the Feynman-diagrammatic approach defined in Ref. [24]. It calculates the virtual corrections to any $2 \rightarrow 2$ process such that it can be applied to the standard model, MSSM, or any other renormalizable theory.

The module uses QGRAF [23], FORM [43], MAPLE, and the GOLEM95 integral library [25] to produce FORTRAN90 code that calculates the virtual cross section for a $2 \rightarrow 2$ process, given a set of phase space points. It also produces analytical MAPLE output in the form of partial amplitudes. Each virtual diagram is broken down according to its color structure, helicity, and scalar integrals. This allows for a careful test before the numerical calculation is even started. The approach can be divided into four main steps:

1. Generate the tree-level diagrams, counterterms, and one-loop diagrams with QGRAF and translate the output into FORM code suitable for symbolic manipulation. The analytic structures keep track of external wave functions, vertex couplings and internal propagators, color factors, Lorentz structure, and the overall sign from external fermions.
2. Map the analytic structures onto partial amplitudes using a basis in color, helicity, and tensor structures using the spinor-helicity formalism.
3. Apply an analytical reduction of tensor integrals to scalar loop integrals based on the GOLEM reduction scheme [24,25].
4. Collect all results and insert the renormalization constants into the counterterms. The final output is available as analytical partial amplitudes in MAPLE and as numerical FORTRAN90 output. The latter is implemented into the MADGRAPH structure.

These four blocks are coordinated and run by the PERL script *run_golem.pl*. We will describe them in detail below.

In the first step QGRAF generates all Born diagrams, counterterms, and QCD one-loop corrections for a hard process specified in a MADGRAPH-like file *proc_card.dat*. QGRAF obtains the topological rules from modified MADGRAPH model files. In addition to the familiar MADGRAPH options, we include novel functionalities specific to a NLO calculation; for instance, the flag *nlotype* in the process card generates either pure QCD (gluon mediated) or full SUSY-QCD virtual corrections. This division relies on a constrained set of propagators within QGRAF. Note that SUSY-QCD corrections also include loop diagrams which do not involve either gluons or gluinos, e.g., mediated by the four-squark vertex. Therefore, QGRAF first includes all loop diagrams with gluons, gluinos, and squarks as well as Faddeev-Popov ghosts. The number of loop diagrams is reduced later by checking the order of α_s.

Counterterms are generated automatically by QGRAF via tree-level diagrams containing placeholders for all renormalization constants. These renormalization constants depend on $\mathcal{O}(\alpha_s)$ corrections to a set of two-point functions involving the different colored particles present within a given model. We provide them as a set of separated (model-dependent) libraries, implemented as MAPLE list files.

Additional topological constraints, e.g., requiring only gluonic t-channel contributions, or only self-energy corrections, can be included via *run_golem.pl*. At this stage the code groups topologically equivalent structures and applies loop filtering techniques, e.g., removing diagrams which are trivially zero. The PERL script also assigns the overall sign to each diagram, because standard QGRAF is not valid for Majorana fermions.

Once the QGRAF output is filtered by *run_golem.pl*, the remaining set of diagrams is processed in FORM to apply Feynman rules. Assigning the correct fermion flow is crucial for diagrams with Majorana particles [44].

The second step of MADGOLEM treats the color and helicity structure of the QGRAF and FORM output. For the

QCD structure of each Feynman diagram FORM uses a color-flow decomposition [45]. Each external gluon is matched with an adjoint generator T^a_{ij}, which means we can rewrite the gauge structure using delta functions in color space, and factorize it from the remaining amplitude. This way the color flow within the amplitude becomes more apparent.

The spin structure of each diagram is also manipulated in FORM. Using the spinor-helicity formalism [46,47] the amplitude is projected onto a set of helicity amplitudes. Each fermion pair and vector boson is rewritten as massless spinor products, of which we take the traces. This way each diagram is expressed in the Mandelstam variables s, t and u, with a spinor product prefactor. Massive spinors require a helicity projection in the direction of an auxiliary reference vector which we choose to be the lightlike momentum of one of the other external particles k_i. Whenever this is not allowed we instead use $k_5 = (E_1 + E_2)(1, 1, 0, 0)/2$. In this case the kinematic structure is no longer defined by the usual Mandelstam variables, so we also include s_{15}, s_{25}, s_{35}, s_{45}, and $i\epsilon_{\mu\nu\rho\sigma}k_1^\mu k_2^\nu k_3^\rho k_5^\sigma$. This additional reference vector seriously impacts the tensor reduction described below and slows down the amplitude generation and evaluation.

In step three of MADGOLEM we simplify the loop diagrams using the GOLEM approach [24,25]. For a fully analytical reduction of tensor integrals to a linear combination of scalar integrals we rely on a combination of FORM and MAPLE. All one-loop integrals are regularized dimensionally; internal momenta and gamma matrices are split into four-dimensional and (-2ϵ)-dimensional components, with the latter only contributing at $\mathcal{O}(\epsilon)$ [48]. Tensor loop integrals we simplified using a Passarino-Veltman reduction [49]. This reduces an N-point tensor integral of rank r to a scalar N-point integral plus a series of integrals with fewer external legs and reduced rank. The final result we can express in terms of known scalar integrals (D_0, C_0, B_0, A_0) in $4 - 2\epsilon$ dimensions. Their divergence structure is simple: IR poles arise purely from D_0 and C_0, and UV poles arise purely from B_0 and A_0. The only exception to this rule is the scalar two-point function

$$\begin{aligned} B_0(0,0,0) &= \int \frac{d^D q}{(2\pi)^D} \frac{1}{q^2(q+p)^2} \\ &= \frac{i}{16\pi^2} \frac{(4\pi)^\epsilon}{\Gamma(1-\epsilon)} \left(\frac{1}{\epsilon_{\rm UV}} - \frac{1}{\epsilon_{\rm IR}}\right), \end{aligned} \tag{C1}$$

which in this schematic notation is IR and UV divergent. Its finite part vanishes, but in our calculation we need to keep track of its IR and UV poles separately. As mentioned above, four-point tensor integrals with $k_5 \cdot l$ in the numerator (l standing for the internal loop momentum) cannot be simplified using the Passarino-Veltman approach and are kept as unreduced form factors to be numerically processed by GOLEM95.

In the final step we collect all partial amplitudes for a given process using MAPLE. Two analytical output files contain all information about the Born amplitude and the renormalized virtual amplitude:

(i) *AMP_TREE.mapout* lists the total nonzero Born amplitudes, sorted by diagram, helicity, and color representation. If the flag *nlosymsimp* is enabled in the MADGRAPH process card, the helicity amplitudes are tested for the possible symmetry $\mathcal{M}^{\{\lambda\}} = \mathcal{M}^{\{\lambda'\}*}$, where $\{\lambda'\}$ is a different helicity from $\{\lambda\}$. Only the minimal set of helicity amplitudes is kept, along with a note of which helicities are conjugates of which. This greatly reduces the size of the output for pure QCD or QED processes.

(ii) *AMP_LOOP.mapout* lists all finite loop amplitudes as kinematic coefficients sorted by diagram, helicity, color representation, and type (scalar integral, form factor, or number). In the same format it also lists the counterterms after the renormalization constants have been inserted. The simplification flag *nlosymsimp* is also applied to the loop amplitudes.

For a numerical evaluation we do not rely on this analytic output. Instead, MADGOLEM writes several FORTRAN90 routines for the computation of the virtual corrections:

(i) *libcoeffs_all.so* and *libcoeffs_all_tree.so* contain the amplitude coefficients for the virtual corrections and Born amplitudes. For size reasons we generate a separate library for each partial amplitude. Each library we pre-compile before linking them dynamically and launching them at runtime.

(ii) *golem(k,mu,amplitude_array)* takes the external four-momenta $k_{1,2,3,4}$ and the renormalization scale μ and returns

$$\text{amplitude\_array} = \left(a_0, \frac{a_{-1}}{\epsilon}, \frac{a_{-2}}{\epsilon^2}, |\mathcal{M}|^2_{\rm Born}, a_{\rm UV}\right). \tag{C2}$$

The different a_j are defined through the interference term between Born and virtual amplitude,

$$\begin{aligned} |\mathcal{M}|^2_{\text{1-loop}} &= 2\,\mathrm{Re}(\mathcal{M}^*_{\rm born}\mathcal{M}_{\rm virt}) \\ &= a_0 + \frac{a_{-1}}{\epsilon} + \frac{a_{-2}}{\epsilon^2}, \end{aligned} \tag{C3}$$

and correspond to the finite contribution (a_0), and the coefficients of the single (a_{-1}) and double (a_{-2}) IR poles. The Born term is included for comparison with MADGRAPH, and $a_{\rm UV}$ returns the numerical value of the UV pole which is zero after proper renormalization. All results are averaged over initial-state colors and helicities.

(iii) *virtual_corrections.f90* contains the subroutine *golem(k,mu,amplitude_array)*, which calls the integral library GOLEM95 and the coefficient libraries *libcoeffs*.so*. It calculates the fully renormalized matrix element at one-loop level. The three values a_0, a_{-1}, a_{-2} are combined with the integrated dipoles from the real emission corrections for the complete NLO corrections to a 2 → 2 process. The cancellation of the single and double poles is automatically checked in our numerical implementation.

As is appropriate for an automized NLO tool we have undertaken an exhaustive program of checks to ensure the robustness and reliability of our MADGOLEM. We have calculated the (SUSY)-QCD one-loop corrections for a large set of 2 → 2 processes both in the standard model and the MSSM, covering all representative possibilities of spins, color charges, interaction patterns, and topologies. The cancellation of the UV, IR, and OS divergences, as well as the gauge invariance of the overall result, can be confirmed numerically, for some specific cases also analytically. The finite renormalized one-loop amplitudes we have systematically compared with FEYNARTS, FORMCALC, and LOOPTOOLS [50].

APPENDIX D: RENORMALIZATION

As discussed in the previous Appendix, we automatically generate the ultraviolet counterterms using the tree-level amplitude from QGRAF. As an input we express all renormalization constants in terms of two-point functions as a separate library. The current MADGOLEM implementation fully supports renormalized QCD effects for the standard model, the MSSM, sgluons [17], and other new physics models. To document our notation we give all relevant expressions for the renormalization of supersymmetric QCD here.

The renormalization constants we define through the relation between the bare and the renormalized fields, masses, and the coupling constant:

$$\begin{aligned} \Psi^{(0)} &\to Z_\Psi^{1/2}\Psi, \\ m_\Psi^{(0)} &\to m_\Psi + \delta m_\Psi, \\ g_s^{(0)} &\to g_s + \delta g_s. \end{aligned} \tag{D1}$$

The field $\Psi = q, \tilde{q}, g, \tilde{g}$ denotes all strongly interacting MSSM fields. We express the SUSY-QCD counterterms to vertices and propagators in Table IV.

The actual counterterms, presented below, we include in a separate library. The strong coupling constant we renormalize in the $\overline{\text{MS}}$ scheme and explicitly decouple all particles heavier than the bottom quark. This zero-momentum subtraction scheme [11,51,52] leaves us with

TABLE IV. Strong interaction counterterms for the MSSM. The finite supersymmetry-restoring counterterm δ_{SUSY} is given in Eq. (D4).

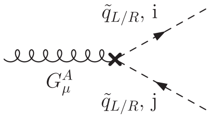	$-ig_sT_{ij}^A\left[\delta g_s + \frac{\delta Z_{\tilde{q}_{L/R,i}} + \delta Z_{\tilde{q}_{L/R,j}} + \delta Z_G}{2}\right]\tilde{q}_{L/R,i}(p_i + p_j)^\mu G_\mu^A \tilde{q}_{L/R,j}$
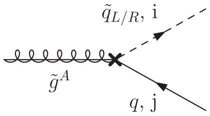	$\mp ig_s\sqrt{2}T_{ij}^A\left[\delta g_s + \frac{\delta Z_{\tilde{q}_{L/R,i}} + \delta Z_{q_j} + \delta Z_{\tilde{g}}}{2} + \delta_{\text{SUSY}}\right]\tilde{g}^A P_{L/R} q_j \tilde{q}_{L/R,i}$
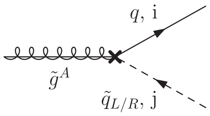	$\pm ig_s\sqrt{2}T_{ij}^A\left[\delta g_s + \frac{\delta Z_{\tilde{q}_{R/L,j}} + \delta Z^*_{q_i} + \delta Z_{\tilde{g}}}{2} + \delta_{\text{SUSY}}\right]\bar{q}_i P_{L/R}\tilde{g}^A \tilde{q}_{R/L,j}$
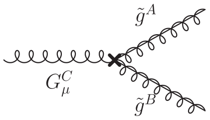	$-g_sf^{ABC}\left[\delta g_s + \delta Z_{\tilde{g}} + \frac{\delta Z_G}{2}\right]\tilde{g}^A\gamma^\mu\tilde{g}^B G_\mu^C$
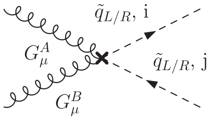	$ig_s\{T^AT^B\}_{ij}\left[\delta g_s + \delta Z_G + \frac{\delta Z_{\tilde{q}_{L/R,i}} + \delta Z_{\tilde{q}_{L/R,j}}}{2}\right]\tilde{q}_{L/R,i}\tilde{q}_{L/R,j}G_\mu^A G^{B\mu}$
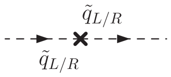	$p^2\delta Z_{\tilde{q}_{L/R}} - m^2_{\tilde{q}_{L/R}}\delta Z_{\tilde{q}_{L/R}} - \delta m^2_{\tilde{q}_{L/R}}$
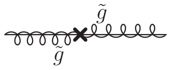	$\not{p}\delta Z_{\tilde{g}} - m_{\tilde{g}}\delta Z_{\tilde{g}} - \delta m_{\tilde{g}}$

the renormalization group running of α_s to light colored particles only. It corresponds to the measured value of the strong coupling, for example in a combined fit with the parton densities. Its renormalization constant reads

$$\delta g_s = -\frac{\alpha_s}{4\pi}\frac{\beta_0^L+\beta_0^H}{2}\frac{1}{\tilde\epsilon} - \frac{\alpha_s}{4\pi}\left(\frac{1}{3}\log\frac{m_t^2}{\mu_R^2} + \log\frac{m_{\tilde g}^2}{\mu_R^2} + \frac{1}{12}\sum_{\text{squarks}}\log\frac{m_{\tilde q_j}^2}{\mu_R^2}\right). \tag{D2}$$

The UV divergence appears as $1/\tilde\epsilon \equiv (4\pi)^\epsilon/\Gamma(1-\epsilon) = 1/\epsilon - \gamma_E + \log(4\pi) + \mathcal{O}(\epsilon)$. Both light ($L$) and heavy ($H$) colored particles contribute to the beta function

$$\begin{aligned}\beta_0 &= \beta_0^L + \beta_0^H\\ &= \left[\frac{11}{3}C_A - \frac{2}{3}n_f\right] + \left[-\frac{2}{3} - \frac{2}{3}C_A - \frac{1}{3}(n_f+1)\right].\end{aligned} \tag{D3}$$

MADGOLEM sets the number of active flavors to $n_f = 5$. The $SU_C(3)$ color factors are $C_F = 4/3$ and $C_A = 3$.

The analytic form of all renormalization constants we reduce down to one-point and two-point scalar one-loop functions, which we handle by means of the standard 't Hooft-Veltman dimensional regularization scheme in $4-2\epsilon$ dimensions. The field and mass renormalization constants we compute from the one-loop self-energies which involve virtual gluons and gluinos. All fields are renormalized on-shell. In addition, for the gluon field we subtract the heavy modes consistently with our g_s renormalization scheme. The underlying Slavnov-Taylor identities link the corresponding finite counterterms as $\delta Z_G = -2\delta g_s$.

In addition, we need to pay attention to dimensional regularization breaking supersymmetry through a mismatch of two gaugino and the $2-2\epsilon$ gauge vector degrees of freedom [30]. As a result, the Yukawa coupling $\hat g_s$ appearing in the $q\tilde q\tilde g$ vertex departs from g_s. We restore supersymmetry by hand, forcing $\hat g_s = g_s$. The corresponding finite counterterm can be computed using dimensional reduction,

$$\frac{\hat g_s}{g_s} = \frac{\alpha_s}{4\pi}\left(\frac{2}{3}n_f - \frac{3}{2}C_F\right) \Rightarrow \delta_{\text{SUSY}} = \frac{4}{3}\frac{\alpha_s}{4\pi}. \tag{D4}$$

Finally, we quote the analytical expressions for the field and mass renormalization. For the scalar one-point and two-point functions we adopt the notation of Ref. [53]. The corrections to the massless quarks including the nonchiral SUSY contributions are

$$\begin{aligned}\delta Z_{q_{L/R}} = -\frac{\alpha_s}{4\pi}C_F\big[&B_0(0,0,0) + B_0(0,m_{\tilde g}^2,m_{\tilde q_{L/R}}^2)\\ &+ (m_{\tilde g}^2 - m_{\tilde q_{L/R}}^2)B_0'(0,m_{\tilde g}^2,m_{\tilde q_{L/R}}^2)\\ &+ (m_{\tilde g}^2 - m_{\tilde q_{R/L}}^2)B_0'(0,m_{\tilde g}^2,m_{\tilde q_{R/L}}^2)\big].\end{aligned} \tag{D5}$$

The corresponding squark fields ($\tilde q_{s=L/R}$) and mass are renormalized as

$$\begin{aligned}\delta Z_{\tilde q_s\tilde q_s} &= \frac{\alpha_s}{2\pi}C_F\big[B_0(m_{\tilde q_s}^2,0,m_{\tilde q_s}^2) + m_{\tilde q_s}^2B_0'(m_{\tilde q_s}^2,0,m_{\tilde q_s}^2)\\ &\quad - B_0(m_{\tilde q_s}^2,m_{\tilde g}^2,0) + (m_{\tilde g}^2 - m_{\tilde q_s}^2)B_0'(m_{\tilde q_s}^2,m_{\tilde g}^2,0)\big],\\ \delta m_{\tilde q_s} &= -\frac{\alpha_s}{4\pi}C_F\big[4m_{\tilde q_s}^2 + 3A_0(m_{\tilde q_s}^2) + 2A_0(m_{\tilde g}^2)\\ &\quad + 2(m_{\tilde g}^2 - m_{\tilde q_s}^2)B_0(m_{\tilde q_s}^2,m_{\tilde g}^2,0)\big].\end{aligned} \tag{D6}$$

The gluon wave function renormalization, linked to the counterterm for the strong coupling, is

$$\delta Z_G = \frac{\alpha_s}{4\pi}(\beta_0^L+\beta_0^H)\frac{1}{\tilde\epsilon} + \frac{\alpha_s}{2\pi}\left[\frac{1}{3}\log\frac{m_t^2}{\mu^2} + \log\frac{m_{\tilde g}^2}{\mu^2} + \frac{1}{12}\sum_{\text{squarks}}\log\frac{m_{\tilde q}^2}{\mu^2}\right]. \tag{D7}$$

Finally, the gluino field and mass renormalization constants are

$$\begin{aligned}\delta Z_{\tilde g} &= \frac{\alpha_s}{4\pi}C_A\left[1 + 4m_{\tilde g}^2B_0'(m_{\tilde g}^2,0,m_{\tilde g}^2) - \frac{A_0(m_{\tilde g}^2)}{m_{\tilde g}^2}\right] + \frac{\alpha_s}{8\pi m_{\tilde g}^2}\sum_{\text{light (s) quarks}}\big[A_0(m_{\tilde q}^2) - (m_{\tilde g}^2 + m_{\tilde q}^2)B_0(m_{\tilde g}^2,0,m_{\tilde q}^2)\\ &\quad - 2m_{\tilde g}^2(m_{\tilde g}^2 - m_{\tilde q}^2)B_0'(m_{\tilde g}^2,0,m_{\tilde q}^2)\big] + \frac{\alpha_s}{8\pi m_{\tilde g}^2}\sum_{\text{heavy (s) quarks}}\big[2m_{\tilde g}^2(m_{\tilde q}^2 - m_q^2 - m_{\tilde g}^2)B_0'(m_{\tilde g}^2,m_q^2,m_{\tilde q_s}^2)\\ &\quad + (m_q^2 - m_{\tilde q}^2 - m_{\tilde g}^2)B_0(m_{\tilde g}^2,m_q^2,m_{\tilde q}^2) + A_0(m_{\tilde q}^2) - A_0(m_q^2)\big] + \frac{\alpha_s}{\pi}\sum_{\text{heavy (s) quarks}}m_{\tilde g}m_qR^q_{s1}R^q_{s2}B_0'(m_{\tilde g}^2,m_q^2,m_{\tilde q_s}^2),\\ \delta m_{\tilde g} &= -\frac{\alpha_s}{4\pi}C_Am_{\tilde g}\left[1 + 3\frac{A_0(m_{\tilde g}^2)}{m_{\tilde g}^2}\right] + \frac{\alpha_s}{8\pi m_{\tilde g}}\sum_{\text{light (s) quarks}}\big[A_0(m_{\tilde q}^2) + (m_{\tilde g}^2 - m_{\tilde q}^2)B_0(m_{\tilde g}^2,0,m_{\tilde q}^2)\big]\\ &\quad + \frac{\alpha_s}{8\pi m_{\tilde g}}\sum_{\text{heavy (s) quarks}}\big[A_0(m_{\tilde q}^2) - A_0(m_q^2) - (m_{\tilde q}^2 - m_q^2 - m_{\tilde g}^2)B_0(m_{\tilde g}^2,m_q^2,m_{\tilde q}^2)\big]\\ &\quad - \frac{\alpha_s}{2\pi}\sum_{\text{heavy (s) quarks}}m_qR^q_{s1}R^q_{s2}B_0(m_{\tilde g}^2,m_q^2,m_{\tilde q_s}^2).\end{aligned} \tag{D8}$$

The sum over heavy squarks covers all squark flavors corresponding to heavy quarks. We usually consider the bottom quark massless, which means that only the two stop eigenstates feel top mass effects. However, the bottom/sbottom loops can be trivially moved from the light to the heavy category. The stop mass eigenstates $\tilde{t}_{1,2}$ are related to the electroweak interaction bases through a rotation with $R = \pm 1$.

[1] D.E. Morrissey, T. Plehn, and T.M.P. Tait, Phys. Rep. **515**, 1 (2012).

[2] G. Aad *et al.* (ATLAS Collaboration), arXiv:1208.0949; Report No. ATLAS-CONF-2012-109, http://cdsweb.cern.ch/record/1472710.

[3] S. Chatrchyan *et al.* (CMS Collaboration), Phys. Rev. Lett. **109**, 171803 (2012); Report No. CMS-PAS-SUS-12-016, http://cdsweb.cern.ch/record/1460095.

[4] J. Jaeckel, V. V. Khoze, T. Plehn, and P. Richardson, Phys. Rev. D **85**, 015015 (2012).

[5] T. Plehn, D. Rainwater, and P.Z. Skands, Phys. Lett. B **645**, 217 (2007); T. Plehn and T.M.P. Tait, J. Phys. G **36**, 075 001 (2009); J. Alwall, S. de Visscher, and F. Maltoni, J. High Energy Phys. 02 (2009) 017.

[6] C. Englert, T. Plehn, P. Schichtel, and S. Schumann, Phys. Rev. D **83**, 095009 (2011).

[7] A. Hook, E. Izaguirre, M. Lisanti, and J.G. Wacker, Phys. Rev. D **85**, 055029 (2012).

[8] G.L. Kane and J.P. Leveille, Phys. Lett. **112B**, 227 (1982); P.R. Harrison and C.H. Llewellyn Smith, Nucl. Phys. **B213**, 223 (1983); **B223**, 542(E) (1983); E. Reya and D.P. Roy, Phys. Rev. D **32**, 645 (1985); S. Dawson, E. Eichten, and C. Quigg, Phys. Rev. D **31**, 1581 (1985).

[9] W. Beenakker, R. Höpker, M. Spira, and P.M. Zerwas, Phys. Rev. Lett. **74**, 2905 (1995); W. Beenakker, M. Krämer, T. Plehn, M. Spira, and P.M. Zerwas, Nucl. Phys. **B515**, 3 (1998); G. Bozzi, B. Fuks, and M. Klasen, Phys. Rev. D **72**, 035016 (2005); W. Hollik, J.M. Lindert, and D. Pagani, arXiv:1207.1071.

[10] W. Beenakker, R. Höpker, M. Spira, and P.M. Zerwas, Z. Phys. C **69**, 163 (1995).

[11] W. Beenakker, R. Höpker, M. Spira, and P.M. Zerwas, Nucl. Phys. **B492**, 51 (1997).

[12] Available under http://www.thphys.uni-heidelberg.de/plehn.

[13] S. Bornhauser, M. Drees, H.K. Dreiner, and J.S. Kim, Phys. Rev. D **76**, 095020 (2007); W. Hollik, M. Kollar, and M.K. Trenkel, J. High Energy Phys. 02 (2008) 018; M. Beccaria, G. Macorini, L. Panizzi, F.M. Renard, and C. Verzegnassi, Int. J. Mod. Phys. A **23**, 4779 (2008); W. Hollik, E. Mirabella, and M.K. Trenkel, J. High Energy Phys. 02 (2009) 002; J. Germer, W. Hollik, E. Mirabella, and M.K. Trenkel, J. High Energy Phys. 08 (2010) 023; J. Germer, W. Hollik, and E. Mirabella, J. High Energy Phys. 05 (2011) 068.

[14] W. Beenakker, S. Brensing, M. Krämer, A. Kulesza, E. Laenen, and I. Niessen, J. High Energy Phys. 12 (2009) 041; J. Debove, B. Fuks, and M. Klasen, Nucl. Phys. **B849**, 64 (2011); A. Kulesza and L. Motyka, Phys. Rev. Lett. **102**, 111802 (2009); Phys. Rev. D **80**, 095004 (2009); M. Beneke, P. Falgari, and C. Schwinn, Nucl. Phys. **B842**, 414 (2011); P. Falgari, C. Schwinn, and C. Wever, J. High Energy Phys. 06 (2012) 052; M.R. Kauth, J.H. Kühn, P. Marquard, and M. Steinhauser, Nucl. Phys. **B857**, 28 (2012).

[15] U. Langenfeld and S.-O. Moch, Phys. Lett. B **675**, 210 (2009); U. Langenfeld, S.-O. Moch, and T. Pfoh, J. High Energy Phys. 11 (2012) 070.

[16] T. Binoth, D. Gonçalves-Netto, D. López-Val, K. Mawatari, T. Plehn, and I. Wigmore, Phys. Rev. D **84**, 075005 (2011).

[17] D. Gonçalves-Netto, D. López-Val, K. Mawatari, T. Plehn, and I. Wigmore, Phys. Rev. D **85**, 114024 (2012).

[18] D. López-Val, D. Gonçalves-Netto, K. Mawatari, T. Plehn, and I. Wigmore, arXiv:1209.2797.

[19] See e.g., G. Cullen, N. Greiner, G. Heinrich, G. Luisoni, P. Mastrolia, G. Ossola, T. Reiter, and F. Tramontano, Eur. Phys. J. C **72**, 1889 (2012); V. Hirschi, R. Frederix, S. Frixione, M. V. Garzelli, F. Maltoni, and R. Pittau, J. High Energy Phys. 05 (2011) 044; G. Bevilacqua, M. Czakon, M.V. Garzelli, A. van Hameren, Y. Malamos, C.G. Papadopoulos, R. Pittau, and M. Worek, Nucl. Phys. B, Proc. Suppl. **205–206**, 211 (2010); for a concise review see also e.g., N. Kauer, Frascati Phys. Ser. **54**, 322 (2012).

[20] J. Alwall, P. Demin, S. de Visscher, R. Frederix, M. Herquet, F. Maltoni, T. Plehn, D.L. Rainwater, and T. Stelzer, J. High Energy Phys. 09 (2007) 028.

[21] J. Alwall, M. Herquet, F. Maltoni, O. Mattelaer, and T. Stelzer, J. High Energy Phys. 06 (2011) 128.

[22] H. Murayama, I. Watanabe, and K. Hagiwara, Report No. KEK-91-11.

[23] P. Nogueira, J. Comp. Physiol. **105**, 279 (1993).

[24] T. Binoth, J.P. Guillet, G. Heinrich, E. Pilon, and C. Schubert, J. High Energy Phys. 10 (2005) 015; G. Cullen, N. Greiner, A. Guffanti, J.P. Guillet, G. Heinrich, S. Karg, N. Kauer, T. Kleinschmidt *et al.*, Nucl. Phys. B, Proc. Suppl. **205–206**, 67 (2010).

[25] T. Binoth, J.P. Guillet, G. Heinrich, E. Pilon, and T. Reiter, Comput. Phys. Commun. **180**, 2317 (2009); G. Cullen, J.P. Guillet, G. Heinrich, T. Kleinschmidt, E. Pilon, T. Reiter, and M. Rodgers, Comput. Phys. Commun. **182**, 2276 (2011).

[26] S. Catani and M.H. Seymour, Nucl. Phys. **B485**, 291 (1997); **B510**, 503(E) (1998); S. Catani, S. Dittmaier, M.H. Seymour, and Z. Trocsanyi, Nucl. Phys. **B627**, 189 (2002).

[27] For some more details see e.g., T. Plehn and C. Weydert, Proc. Sci. CHARGED2010 (2010) 026.

[28] J. Pumplin, D.R. Stump, J. Huston, H.L. Lai, P. Nadolsky, and W.K. Tung, J. High Energy Phys. 07 (2002) 012.

[29] S. Frixione, Z. Kunszt, and A. Signer, Nucl. Phys. **B467**, 399 (1996); Z. Nagy and Z. Trocsanyi, Phys. Rev. D **59**, 014020 (1999); **62**, 099902(E) (2000).

[30] S. P. Martin and M. T. Vaughn, Phys. Lett. B **318**, 331 (1993); A. Signer and D. Stöckinger, Phys. Lett. B **626**, 127 (2005); Nucl. Phys. **B808**, 88 (2009).

[31] S. S. AbdusSalam, B. C. Allanach, H. K. Dreiner, J. Ellis, U. Ellwanger, J. Gunion, S. Heinemeyer, M. Krämer *et al.*, Eur. Phys. J. C **71**, 1835 (2011).

[32] B. C. Allanach, Comput. Phys. Commun. **143**, 305 (2002).

[33] A. Sommerfeld, Ann. Phys. (Berlin) **403**, 257 (1931).

[34] M. L. Mangano, M. Moretti, and R. Pittau, Nucl. Phys. **B632**, 343 (2002).

[35] S. Catani, F. Krauss, R. Kuhn, and B. R. Weber, J. High Energy Phys. 11 (2001) 063.

[36] For a pedagogical introduction see e.g., T. Plehn, Lect. Notes Phys. **844**, 1 (2012).

[37] T. Sjöstrand, S. Mrenna, and P. Z. Skands, J. High Energy Phys. 05 (2006) 026.

[38] H. K. Dreiner, M. Krämer, and J. Tattersall, Europhys. Lett. **99**, 61001 (2012).

[39] R. Frederix, T. Gehrmann, and N. Greiner, J. High Energy Phys. 09 (2008) 122; 06 (2010) 086.

[40] G. Bevilacqua, M. Czakon, C. G. Papadopoulos, R. Pittau, and M. Worek, J. High Energy Phys. 09 (2009) 109.

[41] A. S. Belyaev, E. E. Boos, and L. V. Dudko, Phys. Rev. D **59**, 075001 (1999).

[42] See e.g., S. Frixione, E. Laenen, P. Motylinski, C. White, and B. R. Webber, J. High Energy Phys. 07 (2008) 029.

[43] J. A. M. Vermaseren, arXiv:math-ph/0010025.

[44] A. Denner, H. Eck, O. Hahn, and J. Küblbeck, Nucl. Phys. **B387**, 467 (1992).

[45] F. Maltoni, K. Paul, T. Stelzer, and S. Willenbrock, Phys. Rev. D **67**, 014026 (2003).

[46] Z. Xu, D.-H. Zhang, and L. Chang, Nucl. Phys. **B291**, 392 (1987).

[47] L. J. Dixon, in *Calculating Scattering Amplitudes Efficiently*, Boulder, 1995, (unpublished).

[48] T. Reiter, arXiv:0903.0947.

[49] G. Passarino and M. J. G. Veltman, Nucl. Phys. **B160**, 151 (1979).

[50] T. Hahn, Comput. Phys. Commun. **140**, 418 (2001); T. Hahn and C. Schappacher, Comput. Phys. Commun. **143**, 54 (2002); T. Hahn and M. Pérez-Victoria, Comput. Phys. Commun. **118**, 153 (1999).

[51] S. Berge, W. Hollik, W. M. Mösle, and D. Wackeroth, Phys. Rev. D **76**, 034016 (2007).

[52] J. C. Collins, F. Wilczek, and A. Zee, Phys. Rev. D **18**, 242 (1978).

[53] A. van Hameren, Comput. Phys. Commun. **182**, 2427 (2011).